DEPARTMENT OF PHYSICS

TECHNISCHE UNIVERSITÄT MÜNCHEN

Master's Thesis in Physics

Influence of the charge density on discharges in THGEM-based detectors

Lukas Lautner

DEPARTMENT OF PHYSICS

TECHNISCHE UNIVERSITÄT MÜNCHEN

Master's Thesis in Physics

Influence of the charge density on discharges in THGEM-based detectors

Einfluss der Ladungsdichte auf Entladungen in THGEM-basierten Detektoren

Author:	Lukas Lautner
Supervisor:	Prof. Dr. Laura Fabietti
Advisor:	Dr. Piotr Gasik
Submission Date:	18.11.2019

I confirm that this master's thesis in physics is my own work and I have documented all sources and material used.

Munich, 18.11.2019 Lukas Lautner

Abstract

In Gas Electron Multiplier- and Thick Gas Electron Multipliers-based detectors the discharge stability constrains the safe operating limits in terms of achieved signal amplification. Thus, this is an important optimization parameter for the overall performance of these detectors. The discharge probability is determined for a single THGEM as a function of the absolute gain for various distances between an alpha source and the detector plane in Ar–CO_2 (90–10), Ar–CO_2 (70–30) and Ne–CO_2 (90–10). It is observed that the discharge probability is larger for Ar-based gas mixtures than for Ne-based mixtures and increases with the charge deposition closer to the THGEM. Comparing the measurements with GEANT4 simulations enables the extraction of the critical charge density leading to a discharge in a single THGEM hole for each gas. The critical charge density is determined to be $(2.0 \pm 0.3) \times 10^6$ per hole in Ar–CO_2 (70–30), $(3.5 \pm 0.7) \times 10^6$ in Ar–CO_2 (90–10) and $(5.9 \pm 1.4) \times 10^6$ in Ne–CO_2 (90–10). And thus is consistent with the Raether limit and previous results for GEMs.

Kurzfassung

In Gas Electron Multiplier- and Thick Gas Electron Multipliers-basierten Detektoren setzt die Stabilität gegen elektrische Entladungen Grenzen für den sicheren Betrieb hinsichtlich der erreichbaren Singalverstärkung. Daher ist ein wichtiger Optimierungsparameter für die Gesamtperformance dieser Detektoren. Die Entladungswahrschscheinlichkeit wird für eine einzelne THGEM als Funktion des absoluten Gains für verschiedene Distanzen zwischen Alphaquelle und Detektorebene in Ar–CO_2 (90–10), Ar–CO_2 (70–30) und Ne–CO_2 (90–10) gemessen. Es wird beobachtet, dass die Entladungswahrschscheinlichkeit für Ar-basierte Gasmischungen größer ist als für Ne-basierte und mit der Erzeugung der Primärladung näher an der THGEM wächst. Ein Vergleich der Messungen mit GEANT4 Simulationen erlaubt es die kritische Ladungsdichte, die zu einer Entladung in einem einzelnen THGEM Loch führt, zu bestimmen. Die kritische Ladungsdichte ist $(2.0 \pm 0.3) \times 10^6$ pro Loch in Ar–CO_2 (70–30), $(3.5 \pm 0.7) \times 10^6$ in Ar–CO_2 (90–10) und $(5.9 \pm 1.4) \times 10^6$ in Ne–CO_2 (90–10). Und stimmt folglich mit dem Raetherlimit und vorherigen Ergebnissen mit GEMs überein.

Contents

1 Introduction

Thick Gas Electron Multiplier (THGEM) [1, 2] are modern, robust, high-gain electron multiplier used in gaseous ionization detectors. Its design is derived from the thinner GEM [3] and shares the same working principle of avalanche multiplication within small holes.
During operation of such detectors the exposure to high radiation fluxes or the release of a large amount of charge in the detector volume by a single particle can lead to a breakdown in the gas. These discharges constrain the safe operating limits in terms of achieved gain. The sparks occur after a certain amount of charge has accumulated inside a GEM hole and modified the electric fields accordingly so that a streamer can form [4].
From studies in parallel-plate counters it is known that a breakdown occurs when the number of charges in an avalanche exceeds 10^8, which is the so-called Raether limit [5]. Subsequently, the breakdown limit of micro-pattern gaseous detectors is expected to be of the order of 10^6–10^7 electron–ion pairs [6, 7]. These charge densities can not be created by minimum ionising particle (MIPs) during normal detector operation. MIPs impinging on the detector plane create a low number of primary charges which even at high rates and high gains $>10^3$ do not result in charge densities exceeding the breakdown limit. Of particular interest are therefore highly ionising particles that create high charge densities in the closest vicinity of the detector plane.
In a recent study using heavily ionising alpha particles the critical charge limit in GEMs has been precisely measured and depending on the gas mixture it lies within a range of $4–7\times10^6$ electrons per GEM hole [8]. The measurement of the critical charge limit in the simplest configuration allows for the unbiased extraction of the detector stability against electrical discharges. The result can then be extrapolated to more complex configurations and arbitrary gains. This thesis aims to determine the critical charge limit for a single THGEM setup for different Ar- and Ne-based gas mixtures. To be independent from effects from the presence of transfer fields or charge sharing and spreading between foils no transfer and induction field are used and just the simplest configuration, a single THGEM setup, is studied. To extract the critical charge limit, the measurements are compared to a modified version of the simulation used in [8]. Similar studies also have been performed for Micromegas [9]. With the obtained critical charge values it is then possible to draw a comparison between THGEMs and GEMs regarding their discharge stability.

2 Thick GEM

Gaseous ionization detectors in particle physics were established about 50 years ago with the multi-wire proportional chamber [10]. In such chambers, electron avalanche multiplication occurs around anode wires inside the chamber. In modern detectors the multiplication takes place in more densely structured, patterned electrodes. These types of detectors are typically referred to as Micro-pattern Gaseous Detectors (MPGD), a pioneering example would be the Micro-strip Detector [11]. Similarly, the multiplication in Gas Electron Multiplier (GEM) occurs in small (50-70 µm diameter) holes chemically etched in a 50 µm thin metallized Kapton foil [3]. A thicker version of the GEM, the THGEM, uses the same concept of multiplication in confined volumes [1]. It resembles a GEM with its dimensions expanded by a factor of 5-20 [12]. The larger (sub-)millimeter structures make THGEMs more robust allowing for higher achievable gain than in GEMs, mitigate damage by discharges, and enable the construction of very large detector areas without mechanical support. The larger dimensions make THGEMs also easier to manufacture. The holes are produced by mechanical drilling into a metal-clad insulator for which a variety of PCB materials, like FR-4, Kevlar or Teflon, can be used [13]. Some THGEM variants have the metal around the holes chemically etched which creates metal-free rims surrounding the holes. A close-up of a THGEM with rims can be seen in Fig. 2.1. Adding rims modifies the properties of the THGEM, so is an increase

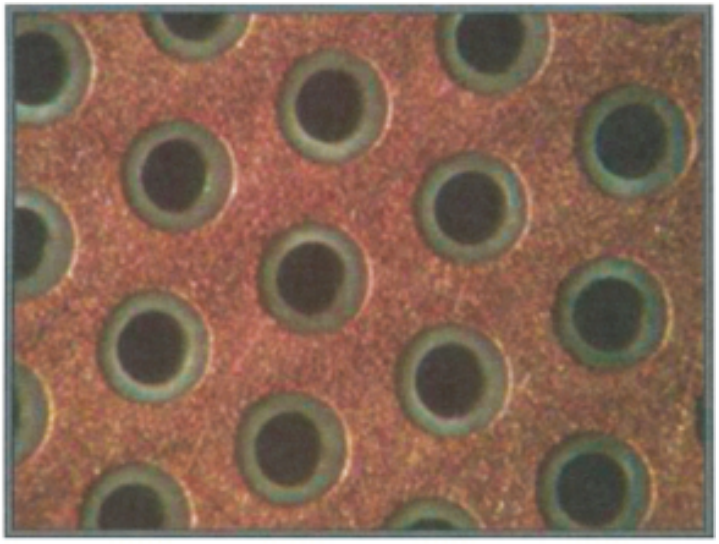

Figure 2.1: Photograph of a THGEM PCB with rims [14].

of the maximum attainable gain with increasing rim size observed, thus also making the

THGEM more stable against discharges at a given gain [13, 15]. Compared to a THGEM without rim the difference in gain can amount up to an order of magnitude [16, 14]. However, rims increase the insulator surface area and are responsible for charging-up and polarization of the substrate material [17].
Like GEMs, THGEMs can be cascaded to increase gain and stability against discharges. THGEMs find use in a wide range of possible applications: For fast-neutron and gamma-ray imaging [18, 19], coated with CsI as photocathode in large area Ring Imaging CHerenkov (RICH) detectors [20, 21] and even as detector in digital hadron calorimeters [22]. Novel concepts use THGEMs as sensing element in cyrogenic noble-liquid TPC for rare-event detection [23, 24, 25, 26]. Further developments include the adaptation to new materials [27] and the combination of different concepts [28].

2.1 Working principle

THGEMs follow the same working principle as GEMs. A potential difference of up to several thousand Volts is applied between top and bottom THGEM electrodes enabling high electric fields inside the THGEM holes. The applied voltage depends on THGEM geometry, gas and desired gain. The electric field in the holes is strong enough to allow for avalanche multiplication. Primary electrons stemming from ionization events in the volume above the THGEM are accelerated by the electric field in the holes such that they reach energies sufficient to ionize further atoms in the medium. In a chain reaction the additional electrons exponentially create further charges resulting in a mixture of positive ions and free electrons in the hole. The detector voltage is chosen so that the created charges are proportional to the initial electrons. The electrons follow the field lines and get extracted towards the bottom electrode while the ions end up on the top electrode. Illustrated in Fig. 2.2 is a simulation in Garfield/Magboltz of two electrons entering the amplification region from the drift region zone of a GEM [29]. In the cross section of the GEM hole it can be seen that the electrons, tracks indicated by yellow lines, get amplified in the high fields within the hole and are mostly extracted towards the bottom direction. The ions that are also created in the avalanche multiplication, tracks indicated by red lines, are collected on the top electrode of the GEM. The collection of ions on the top electrode ensures that only a small fraction of ions are drifting back to the drift volume where they would otherwise distort the drift field, hamper the localization of charges and therefore deteriorating the energy and position resolution of the detector. This showcases the intrinsic ion back flow suppression of a GEM-like detector.

2.2 Charge-up in THGEMs

Gain variations over time in MPGDs incorporating dielectric materials is a well-known phenomenon. It is observed in GEMs [30, 31, 32] as well as in THGEMs [33, 34]. For the former the gain stabilizes within a short period of time in the order of several seconds to minutes [30, 35] whereas for the latter the time until stabilization may even reach days [36]. The gain

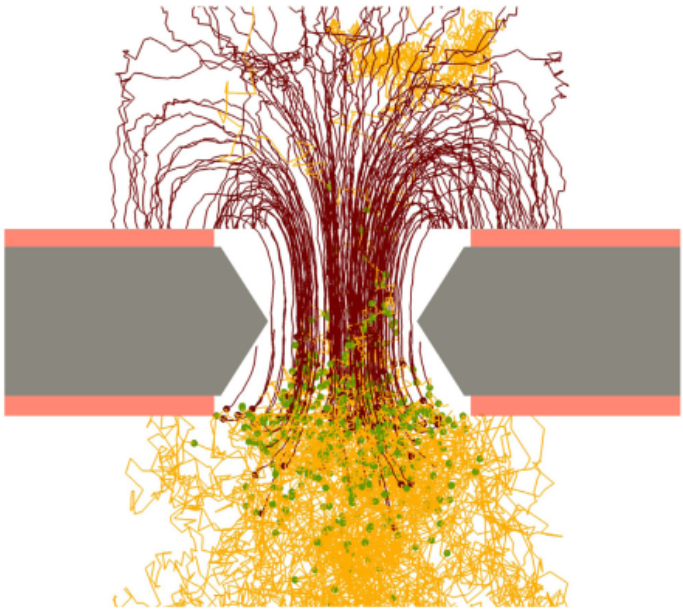

Figure 2.2: Simulation of two electrons arriving and subsequently multiplied in a GEM hole. In red ions and in yellow electron tracks. The green points indicate ionization events. Their paths have been projected on the cross section plane [29].

evolution is governed by the superposition of two electric fields: $E_{uncharged}$, created by the applied potential at the THGEM electrodes and detector geometry and $E_{charges}$ created by charge accumulation on the substrate surface. Hence, the total field is $E_{tot} = E_{uncharged} - E_{charges}$. As $E_{uncharged}$ is externally driven, it remains constant for given experimental conditions. $E_{charges}$ changes over time with the accumulation of charges. After some time the fields will reach an equilibrium and the gain stabilizes.

Charges accumulate on the insulator surface due to the lateral diffusion of the avalanche charge. As shown in Fig. 2.3 positively charged ions from amplification process accumulate at the upper part of the THGEM hole walls whereas the avalanche electrons populate the lower part [37, 38]. These charges create an electric field opposite to the external field and thus reduce the gain. In THGEMs with rims additional substrate is exposed at the top and bottom around the holes. The top rim is then charged negatively by primary electrons that are not reaching the hole. Therefore the charge-up time of the top rim is proportional to the initial charges created by ionization events in the drift volume. At the bottom rim avalanche ions that are created close to the bottom may deviate from the field lines and accumulate on the bottom rim. Thus, the charge-up time of the bottom rim and the THGEM hole walls depends on the final number of charges created by the avalanche process. The amount of exposed substrate surface is therefore the decisive factor for the size of the effect. Charge-up in THGEMs is therefore more pronounced for thickness and increases with the size of the rims. Furthermore a direct linear dependency between the stabilization time and the irradiation

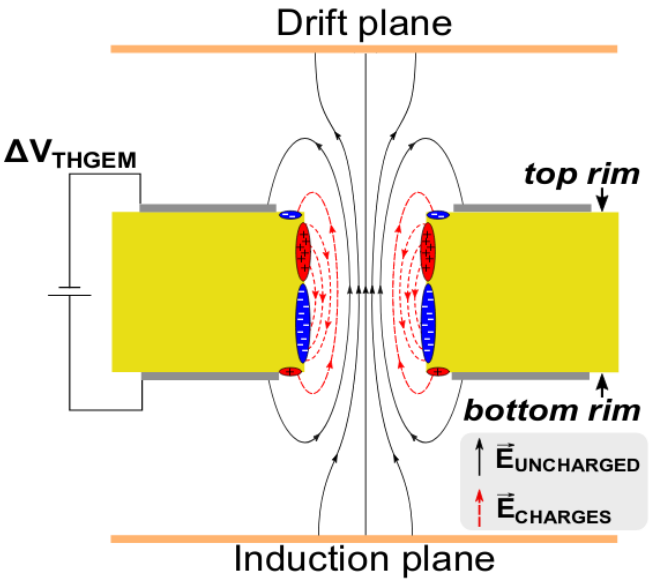

Figure 2.3: Sketch of the charging-up of a THGEM. The initial electric field (black) defined by ΔV_{THGEM} is superimposed by the electric field created by the accumulated charges (red) on the insulating surfaces of the detector [37].

rate of the detector is found. This comes from the fact that the amount of ionization events in the drift gap dictate the rate of initial charges arriving on the rim as well as the multiplied charges within the hole. Since the time until a equilibrium is reached depends on the total charge that passes through a THGEM hole, a inverse proportionality to the detector gain can be observed [37]. Furthermore, the polarization of the insulator volume which leads to moving charges inside the insulator may also play a role for the gain stability [33]. Moreover, experimental conditions unrelated to the THGEM, e.g humidity or impurities in the gas, may influence the stabilization time.

3 Discharges in THGEMs

A discharge is a breakdown of the voltage in a dielectric between two electrodes which allows current to flow between them and thus temporarily or permanently shorts them [39, 40]. In MPGDs electrical discharges are among the leading factors limiting the performance that can be achieved during stable operation. In case of GEM and THGEM discharges may happen in the holes of the foil itself or following a discharge in a hole also between THGEMs or THGEMs and the anode. The former are called primary discharges, the latter secondary or propagated discharges.

3.1 Primary discharges

A primary discharge is marked by a spark which is created by the streamer mechanism [39, 4].
Due to the avalanche multiplication in the GEM a spatially distributed charge cloud consisting of electrons and positive ions, the space charge, is created within a GEM hole. If the combination of the external electric field in the GEM hole and the modification of the electric field by the space charge is strong enough, an electrical breakdown can occur. This goes under the name of streamer condition. For the electric field modification to be strong enough to cause discharges some limit of space charge has to be reached. This limit is the commonly named Raether limit of about 10^8 electron-ion pairs for the parallel plate configuration [5]. The Raether limit is not a constant value but rather depends on the gas composition and geometry of the detector. It has been shown for standard GEMs that this critical charge is the driving mechanism behind primary discharges and is sensitive to the gas mixture. In Ar–CO_2 (90–10) the critical charge has been found to be $(4.7 \pm 0.6)\times10^6$ while in Ne–CO_2 (90–10) it is $(7.3 \pm 0.9)\times10^6$ [8].
The positive ions can be considered as static at the prevalent time scale on the order of nanoseconds whereas the electrons possess a high mobility leading to the formation of a conductive channel spearheaded by negative charges. This channel of ionization is called streamer. Some electrons diffuse against the drift and enhance the field distortion, so that the streamer develops from the GEM bottom electrode (anode) to the GEM top electrode (cathode). The streamer thus propagates "backwards" although the electrons move on average towards the anode [4]. The high concentration of charge at the front of the streamer lead to further ionisation and excitation of gas molecules. Recombination of positive ions and electrons lead to the emission of photons which in turn generate secondary electrons via photo ionization. These processes drive the rapid development of a conductive channel across the whole GEM hole.

After their last ionisation electrons are no longer affected by the strong electric field inside the GEM hole and are able to escape towards the next electrode. The creation of a highly conductive channel between the top and bottom electrodes of the foil in turn eliminates the potential difference. As the electric field within the hole vanishes the discharge is quenched. Through discharges the energy stored in the GEM is released in the GEM hole which heats the gas in the hole and damages the copper layers and PCB material.

As such damages as well as the induced detection dead times are undesirable for the operation of a detector measures to mitigate primary discharge have been developed. These include the stacking of GEM foils to spread the charge and the segmentation of the GEM area so that the effects of the discharge is reduced and limited to one segment. As well as proper decoupling of all GEM electrodes from the power supply by resistors and in cases of THGEM the increase of the rim size to reduce edge effects in the holes.

3.2 Secondary discharges

After a primary discharge a secondary discharges in the gap between two different THGEMs or between a THGEM and the anode may occur. Secondary discharges appear after a primary discharge. They are generally characterized as more violent than primary discharges due to the discharge affecting not only a single THGEM hole but a larger gap.
Due to their appearance at electric fields that are supposed to be too low to lead to a discharge by established mechanisms [41, 42] and the unusual times ($\mathcal{O}$(µs)) between primary and secondary discharge which also exclude a photon-assisted streamer mechanism the secondary discharges are not yet fully understood. Although recently interest in this phenomenon picked up [40, 43] and several hypothesis are available [44] no conclusion to the exact cause has yet been found.
Similar to primary discharges secondary discharges can not be completely avoided but only mitigated by segmentation of the GEM electrodes and optimization and introduction of new RC-components [40, 45]. In the setup used in this work secondary discharges are not expected as there is no field below the THGEM.

4 Experimental setup

4.1 Detector setup

The experimental setup consists of a single THGEM mounted between a drift electrode and a readout anode (Fig. 4.1). In 4.2 a schematic of the setup can be seen. The gap between the drift electrode and the THGEM is called drift gap and is varied between 13.0 mm and 69.5 mm in these studies. The gap below the THGEM (induction gap) is set to 2 mm throughout all measurements.
The $11.2 \times 11.2\,\mathrm{cm}^2$ THGEM itself is produced by Eltos S.p.A. [46] and is divided into three segments. Each segment measures $11.2 \times 3.7\,\mathrm{cm}^2$ with a 600 µm gap between the segments and a hole with an diameter of 4.6 mm in the center of the middle segment. In total this translates into a surface of $123.9\,\mathrm{cm}^2$ covered with copper for the THGEM. This prototype follows the design of the R&D studies for the COMPASS RICH1 Upgrade[47]. The THGEM is 470 µm thick including a 35 µm thick copper layer on each side. The diameter of the holes is 400 µm except for the last row of holes along the side of the THGEM which have a diameter of 500 µm. There is no rim around the holes. The pitch between holes is 800 µm. A picture of the THGEM used in these studies taken under a microscope is shown in 4.3. Clearly visible are a segment boundary and the central mounting hole as well as the hexagonal hole pattern.

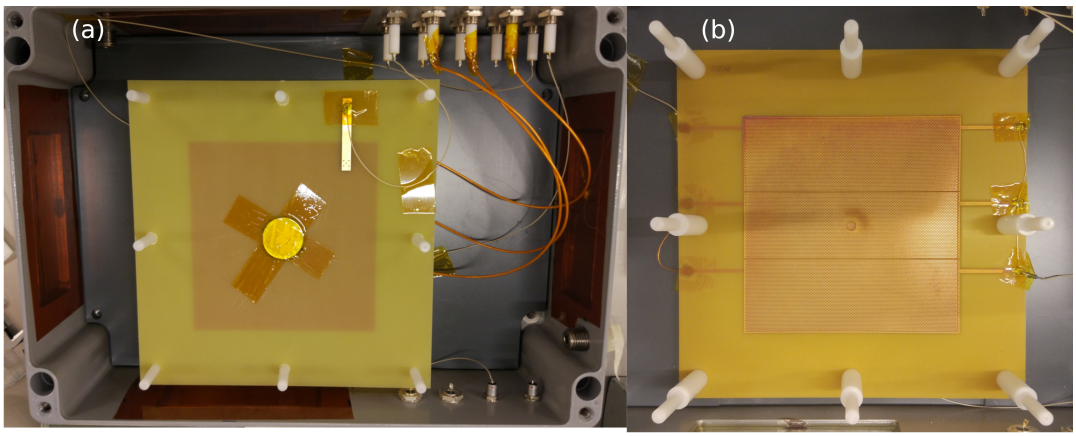

Figure 4.1: Top view of the detector inside with (a) and without (b) mounted cathode and source.

The detector is operated with a drift field (E_{drift}), defined by the potentials at cathode and THGEM top electrode, of $400\,\mathrm{V\,cm}^{-1}$. E_{drift} influences the diffusion and drift properties in

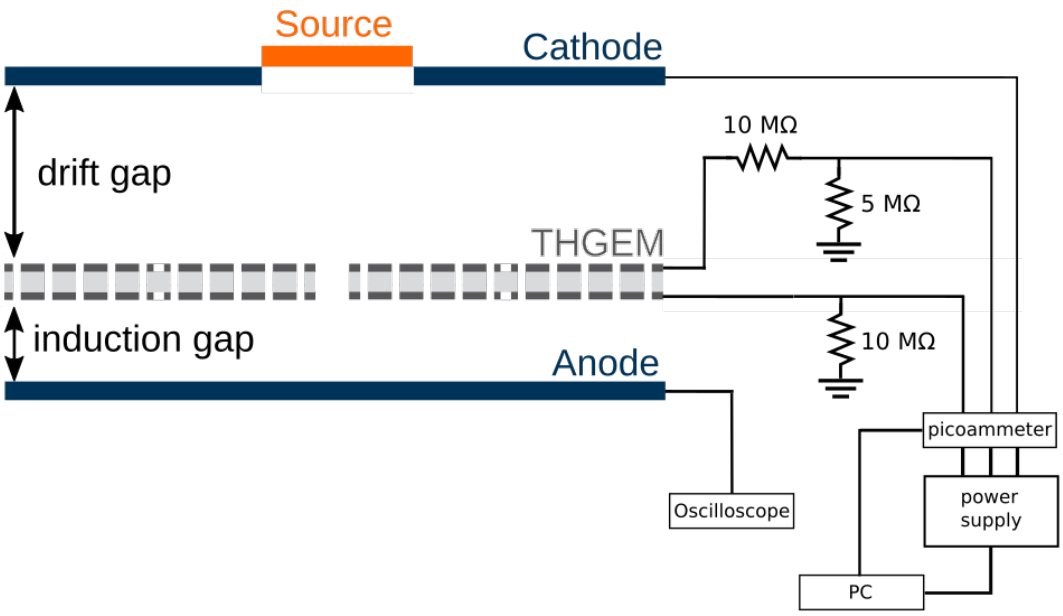

Figure 4.2: Schematic of the detector setup. A single segmented THGEM is mounted between a drift electrode and a readout anode. All electrodes except the anode are read out by a pico–amperemeter. The anode is connected to an oscilloscope.

a given gas mixture, as it is discussed in section 4.1.2. The detector operates without an induction field to exclude any effects of it on the discharge measurements and to determine the absolute gain. A 5 MΩ resistor to ground is connected in series to the top electrode to ensure a constant current. This means that when the current limit of the power supply is exceeded and the power supply shuts down a safe discharge of the THGEM is guaranteed. An additional 10 MΩ protection resistor is directly soldered on the top electrode and connected in series to the power supply. It quenches primary discharges limiting the damage to the THGEM. The potential difference ΔU_{THGEM} across the THGEM is defined by a potential applied to the top electrode. The bottom side of the THGEM is kept at ground potential by the power supply for measurements with a drift gap of 23 mm and 35.5 mm. In these cases, a 10 MΩ resistor to ground is connected in series to the bottom electrode. For all other measurements the bottom electrode is connected directly to ground. The voltages are applied with independent channels using the high voltage power supply ISEG EHS F 060nILK.
To count the signal induced by a discharge the pad plane is read out by an oscilloscope. To determine the absolute gain all electrodes except the anode are read out by a floating multi-channel picoammeter [48]. Detector and picoammeter are both contained inside a large copper box in order to shield the setup from external influences (Fig. 4.4). It is ensured through constant monitoring that the oxygen concentration is always below 25 ppm and humidity does not exceed 200 ppmV H_2O.

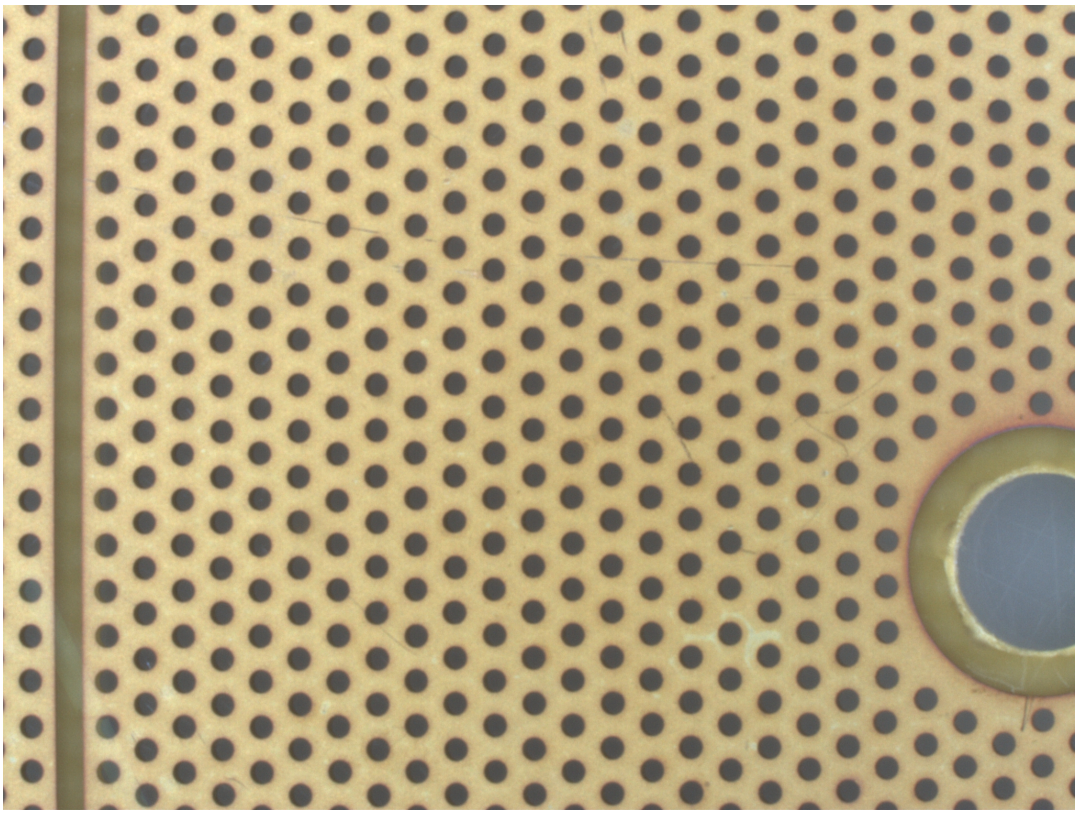

Figure 4.3: Microscope photograph of the THGEM used in this study. The hexagonal pattern of the THGEM holes as well as the central mounting hole and segment boundary can be clearly seen.

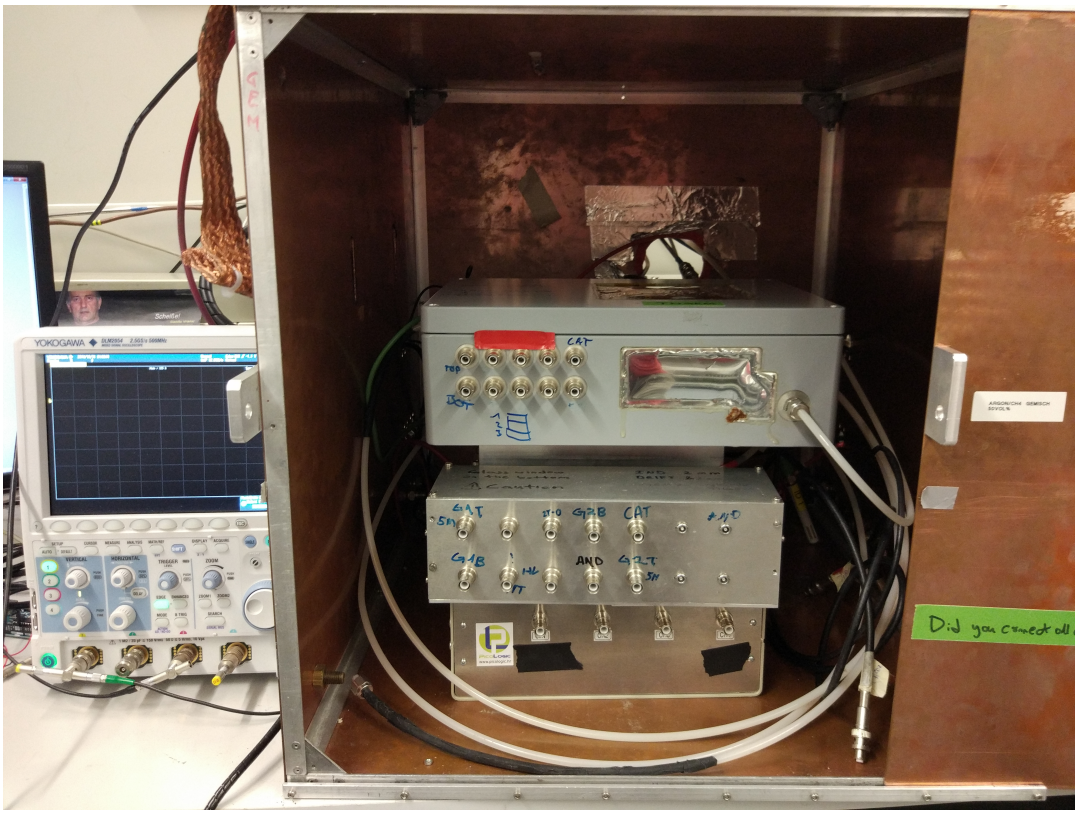

Figure 4.4: Photo of the whole setup. Detector vessel (top) and picoammeter (bottom) in a disconnected state inside the shielding copper box. Oscilloscope for discharge signal readout to the left.

Radionuclide	Energy [MeV]	Intensity [%]
^{239}Pu	5.105	11.5
	5.143	15.1
	5.155	73.4
^{241}Am	5.388	1.4
	5.442	12.8
	5.486	85.2
^{244}Cm	5.763	23.3
	5.805	76.7

Table 4.1: Energies and intensities of the most intense alpha particles emitted by the different nuclides of the radioactive source.

4.1.1 Radiation source

A mixed alpha source containing ^{239}Pu, ^{241}Am and ^{244}Cm is placed on top of the cathode to irradiate the drift volume. The source measures 25 mm in diameter, 0.5 mm in height and the

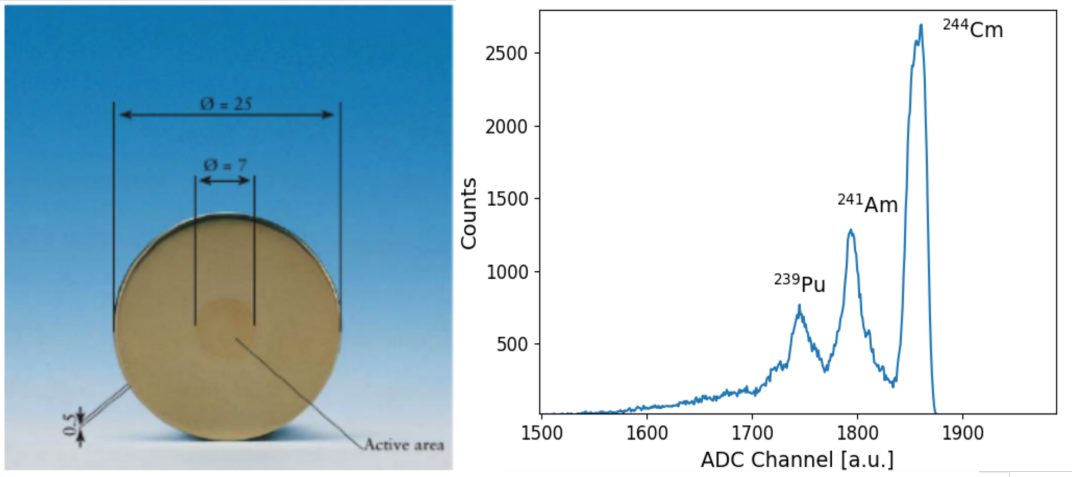

Figure 4.5: The dimension of the mixed alpha source and its measured spectrum in Ne–CO_2 (90–10).

diameter of its active area is 7 mm . The source is placed on a 7 mm hole in the 1.5 mm thick cathode PCB. A picture of the source and its spectrum can be seen in Fig. 4.5. The source emits alpha particles with weighted energies of 5.155 MeV for ^{239}Pu, 5.486 MeV for ^{241}Am and 5.805 MeV for ^{244}Cm [49]. The exact energy distribution can be found in Tab. 4.1. The source rate measured by the detector is 75$\pm$0.3 Hz.

Gas	v_{drift} [cm µs^{-1}]	D_{L} [$\sqrt{\text{cm}}$]	D_{T}[$\sqrt{\text{cm}}$]	W_{i} [eV]
Ar–CO_2 (70–30)	0.932	0.0138	0.0145	28.1
Ar–CO_2 (90–10)	3.25	0.0244	0.0268	28.8
Ne–CO_2 (90–10)	2.66	0.0219	0.0223	38.1

Table 4.2: Table of the properties of gas mixtures used in this study. The electron drift velocity and diffusion coefficients are evaluated at Normal Pressure and Temperature (NTP) conditions at a nominal electric field of 400 V/cm in the absence of a magnetic field.

4.1.2 Gas mixtures

Three different gas mixtures are used in this thesis: Ar–CO_2 (70–30), Ar–CO_2 (90–10) and Ne–CO_2 (90–10). All commonly used mixtures in gaseous ionization detectors. Ar–CO_2 (70–30) is for example used in the TOTEM T2 telescope [50] and COMPASS tracker [51], the PANDA straw tube tracker will operate in Ar–CO_2 (90–10) [52] and Ne–CO_2 (90–10) is used in the ALICE TPC [53]. Argon and neon are noble gases and thus have closed shells, low electron attachment and are chemically non-reactive. Noble gases are single atom gases that do not have any rotational or vibrational states which could absorb electron energy. Therefore, the avalanche process starts in noble gases at lower voltages than in other gases. The mobility of Ar^+ ions is three times lower than that of Ne^+ in neon [54] favoring the buildup of space-charge which may distort electric fields that are present. On the one hand, the effective ionisation potentials W_{i} is higher in Ne-based mixtures than in Ar-based mixtures thus creating less primary charges and requiring a higher gain to achieve the same signal pulse height. On the other hand, this makes Ne-mixtures more stable against discharges. The by traversing particles ionized and excited atoms deexcite via radiative transitions emitting UV photons with energies too low to ionize the detector gas. The photons can then create free charges on metallic surfaces in the detector through the photoelectric effect which could potentially lead to new avalanches in different locations. Created ions drift to the cathode and neutralize there by extracting an electron and emitting UV photons or possible extracting even a second electron. These processes increase the risk of additional avalanches and discharges. To mitigate the effect of the processes above a quenching gas is added. Quenching gases are molecular gases and thus have rotational or vibrational states which can absorb UV photons and transfer charges with noble gas ions due to their lower ionization potential. Although the so created molecule ions also neutralizes at the cathode they will dissociate there without extracting electrons. Common choices for the quenching gas are CH_4, CF_4 and CO_2 of which CO_2 has the lowest cost and also the advantage of being less harmful to the climate and nonflammable.
The gas properties for the given E_{drift} of 400 V cm^{-1} at Normal Pressure and Temperature (NTP) conditions and without magnetic field are summarised in Tab. 4.2. The electron drift velocity v_{drift}, longitudinal (D_{L}) and transverse (D_{T}) diffusion coefficients, and the effective ionisation potentials W_{i} are evaluated using Magboltz [55].

4.2 Data preparation

The cathode and THGEM electrodes are all connected to a 4-channel picoammeter from PicoLogic in series with the power supply [48]. The current is measured for every channel by a picoammeter board which digitalises the data and sends it via optical fibre to an external FPGA board. The data rate of the connection is 500 kbps, while the sampling frequency is 1 kHz.
The FPGA board further processes the data from all picoammeter boards and sends it to the laboratory PC. Even though the measurement setup should be sufficiently shielded from possible interference with the main power grid, a 50 Hz noise filter is applied by the FPGA. Similarly, to enhance the resolution of the current measurement, an additional low-pass filter is used. The FPGA board sends then the preprocessed data to the laboratory computer via USB.
There a LabView application further processes the data and takes over the communication

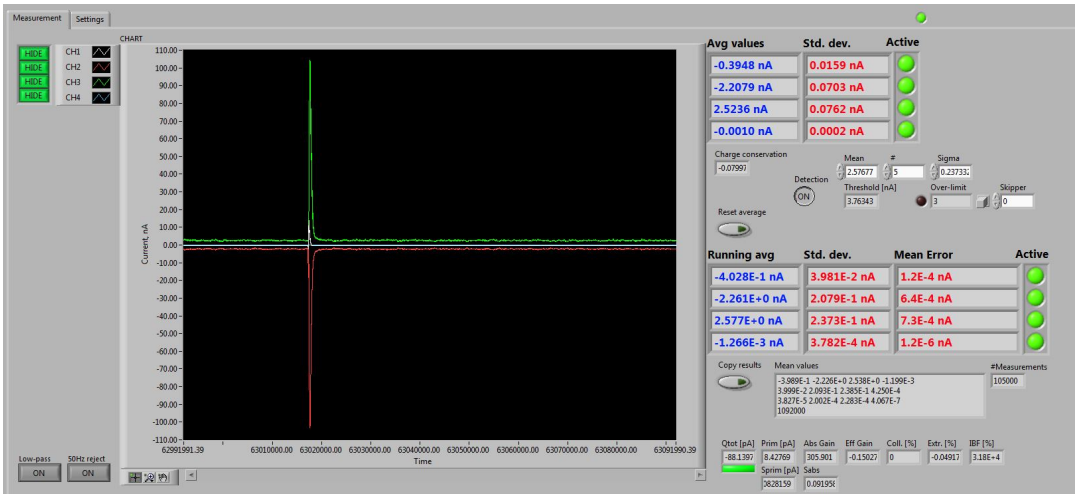

Figure 4.6: Screenshot of the LabView application during measurement. A discharge can be seen in the observed current channels, represented by a distinct peak in the currents of the THGEM top (I_{top}, in red) and bottom (I_{bot}, in green) electrode.

with the FPGA. LabView libraries are distributed together with the picoammeter. The Labview program provides a graphic interface to some functionality of the FPGA like the mentioned low-pass and 50 Hz filters and also implements further capabilities. For all measurements the low-pass and 50 Hz filter are activated. In Fig. 4.6 the user interface of the LabView software is pictured.
To achieve the best possible precision an offset calibration is carried out in two steps before each measurement. Using two steps further reduces the uncertainties on the current measurement as larger signals corresponds to higher uncertainties. At first a zero calibration is done in which for about 2 s the current of all connected channels is recorded and the averaged difference to zero is then subtracted from all channels for all future measurements. The typical difference to zero is of the order of 10^{-3} nA. As second step an offset measurement is

conducted for about 20 min. The averaged offset, around 10^{-4} nA with a standard deviation of $\sim 10^{-7}$ nA, will be then again subtracted from all future measurements.
After the calibrations the offset-corrected current of each channel is stored together with a timestamp in log files for all future measurements. For a proper gain determination the currents of the top and bottom electrode need to be precisely known. This is ensured by measuring long enough so that the standard error of the mean (SEM) σ_{SEM} reaches the order of $\mathcal{O}(10^{-7}\mathrm{nA})$. The SEM is calculated by dividing the standard deviation σ by the square root of the number of measurements N (equation 4.1).

$$\begin{aligned} \sigma &= \frac{1}{\sqrt{\mathrm{N}}} \sum_{i=0}^{N} (x_i - \bar{x}_i)^2 \\ \sigma_{\mathrm{SEM}} &= \frac{\sigma}{\sqrt{\mathrm{N}}} \end{aligned} \tag{4.1}$$

The log file contains occasional write errors scaling with the rate the data is written. A balance between write errors and transfer rate is found to be at 1 Hz. However, this low rate which is imposed by the LabView application is sufficient for its purpose of determining the gain of the very first measurements where charge-up plays a role. Due to the write errors and time format in the log file the log files need to be preprocessed and this is done by a python script. The write errors overwrite and shift lines so that from the overwritten line the first entry persists and the next line begins as second entry of the overwritten line. The script exploits the time stamp format which leads difference of several orders of magnitudes in the numeric values of time (first entry) and currents (subsequent entries). A write error is detected if the value of the second entry of a line lies between the values of the first entry of the previous and next line. The write error gets resolved by shifting the second and all following entries of the affected line by one entry. The script then converts the *ddddhhminminss.msmsms* time code of the log file into seconds and subtracts the time offset so that every measurement starts at zero. The total measurement time used for the calculation of the discharge probability is also determined by this script. An example of a preprocessed measurement can be seen in Fig. 4.7.

4.3 Determination of the absolute gain

All measurements of the discharge probability are performed as function of the absolute gain $\mathrm{G_{abs}}$ of the THGEM. The absolute gain itself is measured as function of $\Delta \mathrm{U}_{THGEM}$. Gain as function of the voltage across the GEM electrodes exhibits an exponential behavior. However, in THGEMs an exponential trend fails to fully describe the $\Delta \mathrm{U}_{THGEM}$-$\mathrm{G_{abs}}$ curve since the gain drops at higher gains and then rises again back to the trend level. This drop coincides with the occurrence of discharges but can not be explained by a bias on the measured currents introduced through discharges [56]. Therefore an extrapolation of the absolute gain towards high gains is not possible and the absolute gain has to be precisely measured for each measurement point. For a more detailed discussion of this phenomenon, see chapter 6.1.

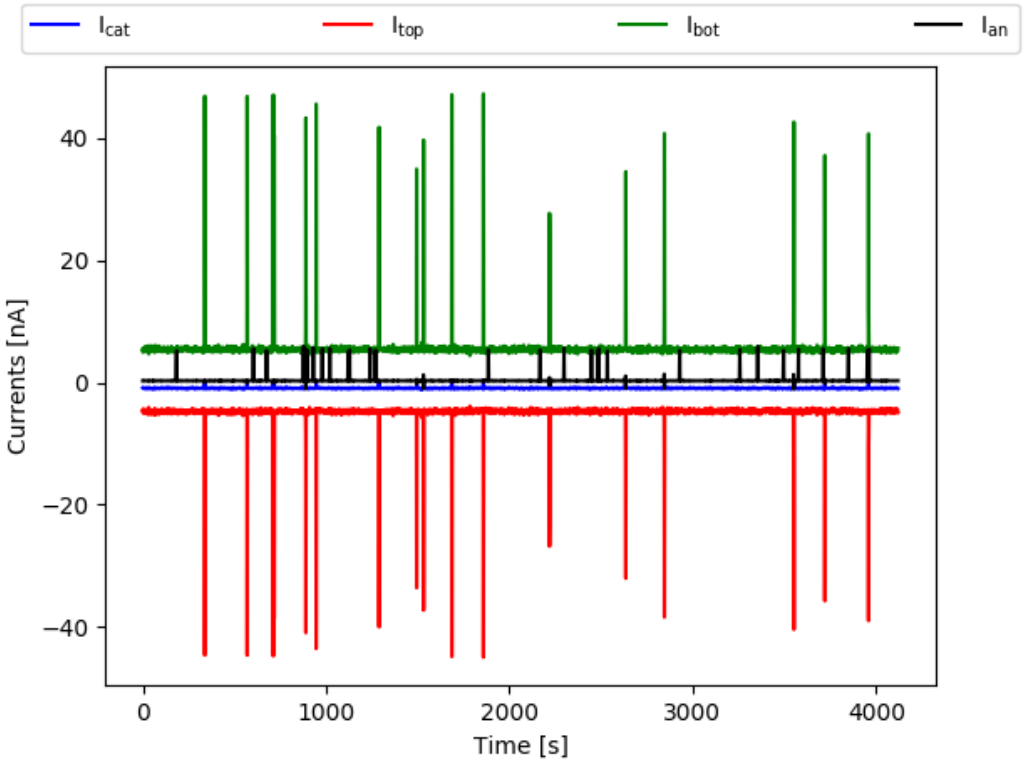

Figure 4.7: Preprocessed currents of all electrodes as a function of time. Several discharges can be easily recognized in I_{top} and I_{bot}. Large signals in the anode current I_{an} are noise picked up by the connection.

For GEMs and THGEMs a distinction is made between the absolute and the effective gain G_{eff}:

$$G_{\text{eff}} = \epsilon_{\text{coll}} \cdot \epsilon_{\text{extr}} \cdot G_{\text{abs}} \tag{4.2}$$

G_{eff} is considering the electron collection ϵ_{coll} and extraction efficiencies ϵ_{extr}. To prevent potential focussing effects which could enhance the charge density inside a THGEM hole and thus influence the discharge probability. All measurements are done without induction fields. As $E_{ind} = 0$ all electrons produced in an avalanche within a THGEM hole are then collected on the bottom electrode. The extraction efficiency to the readout plane is therefore $\epsilon_{extr} = 0$. For standard GEMs with a drift field of $400\,\mathrm{V\,cm^{-1}}$ it can be assumed that all primary electrons reaching the GEM are collected inside the holes [57]. It is assumed that is also the case for THGEMs so that the collection efficiency $\epsilon_{coll} = 1$. The absolute Gain is defined as the ratio of the amplification current at the bottom electrode I_{bot} and the primary current I_{prim}, see equation 4.3.

$$G_{\text{abs}} = \frac{I_{\text{bot}}}{I_{\text{prim}}} \tag{4.3}$$

The primary current is measured at the top electrode with bottom and readout electrode grounded, $\Delta U_{THGEM} = 0$ and a potential applied to the cathode so that a drift field of $400\,\mathrm{V\,cm^{-1}}$ is created. The primary current denotes the current that stems from the electrons which are created in the drift volume by the radiation source and reach the THGEM. The measured primary current ranges from 3 pA to 15 pA with an uncertainty in the order of 10^{-4} pA. To reach the necessary statistics for this high precision the I_{prim} measurements are conducted for about 20 min. The uncertainty of the absolute gain ΔG_{abs} is calculated as follow:

$$\Delta G_{\text{abs}} = G_{\text{abs}} \times \sqrt{\left(\frac{\sigma_{I_{\text{bot}}}}{I_{\text{bot}}}\right)^2 + \left(\frac{\sigma_{I_{\text{prim}}}}{I_{\text{prim}}}\right)^2} \tag{4.4}$$

Discharges in the THGEM constitute a short between the top and bottom electrode and as such lead to temporarily higher currents on those electrodes. These current spikes would introduce a bias towards higher absolute gains. To exclude such a bias currents exceeding $5\,\sigma_{I_{\text{bot}}}$ are not taken into account for calculations of the absolute gain by the LabView software, see Fig. 4.8 for an illustration of this concept.

As discussed in chapter 2.2 charge-up is an issue in THGEMs. Especially in the first measurements of the day when voltage is applied to the THGEM for the first time. As the measurements are progressing from low to high ΔU_{THGEM} respectively from lower to higher gain the charge-up affects the low gain measurements the most. In order to avoid disproportionately long waiting times charge-up effects are corrected by an exponential fit using the preprocessed current log files. A simple exponential fit is employed

$$G_{\text{abs}}(t) = G_0 + \Delta G \cdot e^{-\frac{t}{\tau}}\,. \tag{4.5}$$

The offset G_0 corresponds to the final value of the stabilized gain for $t \to \infty$ and is thus taken as value of G_{abs}. ΔG is the gain drop by which the initial gain is reduced. τ is the

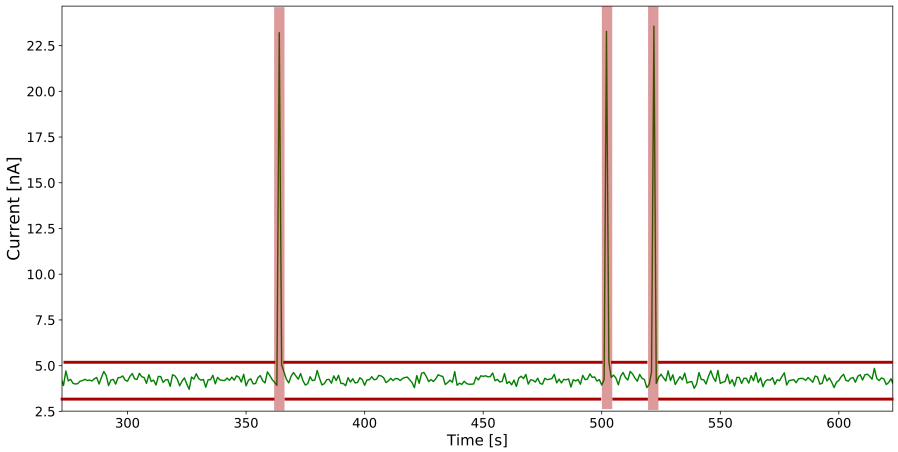

Figure 4.8: Illustration of the rejection of data above 5σ of the I_{bot} current. In between the red lines the current is within five standard deviations of the mean. When the current exceeds or undercuts this limit (vertical bars) the data is not taken into the average.

characteristic time of the decay. The stabilization time $t_{stab} = 5\tau$ describes the time until the gain can be considered stable. For the THGEM used in this study in Ar–CO_2 (90–10) and very low absolute gains ($\lesssim 10$) typical values of τ are in the order of 15 min. For slightly higher gains ($10 \lesssim G_{abs} \lesssim 20$) already significantly lower values around 5 min can be found (Fig. 4.9). τ and thus t_{stab} are proportional to the irradiation rate and inverse proportional to the detctor's gain [37]. Thus, with increasing gain the shape of the gain curve gets more and more flat and the simple exponential fit delivers progressively worse results until it finally fails to describe the data. Therefore in cases where the fit fails and/or the gain values from the LabView application are within the uncertainties of the fit, the extracted gain from the fit is disregarded and the absolute gain from the LabView program is instead taken. Since the LabView software is not bottlenecked by the data rate of 1 kHz compared to the 1 Hz of the log file, the available higher statistics go along with significantly less statistic uncertainty (factor $\sqrt{1000} \sim 31.6$). In the regime of high discharge probability respectively high discharge rate and high gain the low statistics log files do not allow to extract a stable baseline with sufficient precision. Therefore the higher statistics only provided by Labview also enable to reliably probe high absolute gain values. The combination of the exponential fit for low absolute gains and the LabView processing for the other allows to maximize the precision of the absolute gain. With a typical relative uncertainty of below 0.1% for the absolute gain extracted by LabView and below 0.5% for gain value from the exponential fit the absolute gain can be determined with a precision more than sufficient to be used as an input for the discharge probability curves.

The relative standard deviation of the absolute gain for single discharges, i.e. the gain taken

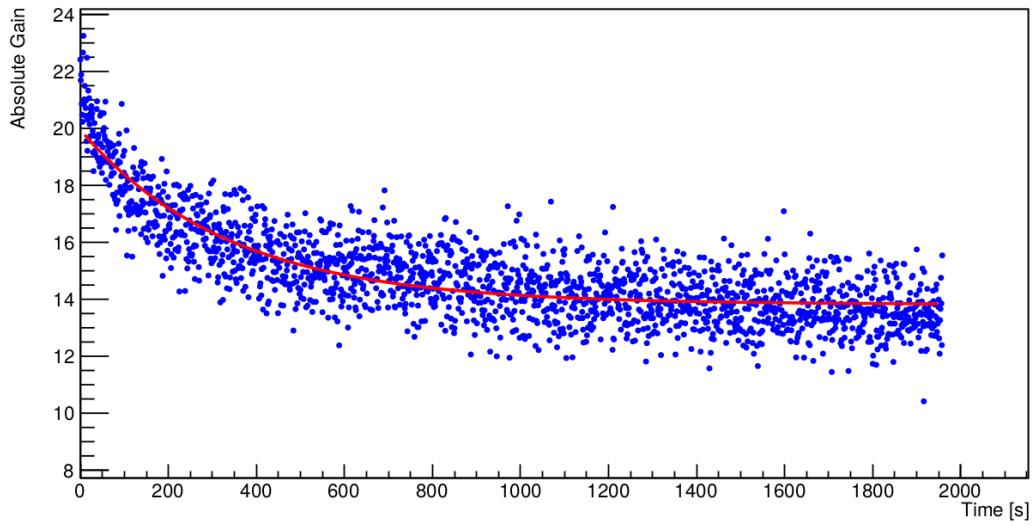

Figure 4.9: Absolute gain as a function of time in Ar–CO_2 (90–10) (blue points). The exponential decay is clearly visible and fitted with a characteristic time of 336 s (red line).

from a baseline interpolation from the absolute gain before and after the discharge, is rather small (< 0.5%) and all gains lie within the statistical uncertainties of the data provided by the log files. Thus an absolute gain determination for each single discharge is not necessary and due to the shortcomings of the log file could also not be reliable conducted for every measurement. So for every discharge in a measurement the averaged absolute gain for this measurement is taken.

4.4 Discharge probability

The discharge probability is observed as function of the absolute gain for different distances to the source. It quantifies the likelihood of the occurrence of a discharge in the THGEM during operation caused by an alpha particle emitted from the radioactive source. The discharge probability P is therefore defined as follows:

$$P = \frac{N}{t \cdot R} \tag{4.6}$$

Where N is the number of discharges, t the time of measurement and R the rate of the radioactive source. Electrical signals of the discharges are read at the anode and captured by an oscilloscope. The uncertainty of the discharge probability is calculated by assuming that

the discharge occurrence is Poisson distributed, shown in equation 4.7.

$$\Delta P = \frac{N}{t \cdot R} \times \sqrt{\left(\frac{\sqrt{N}}{N}\right)^2 + \left(\frac{\Delta R}{R}\right)^2} \tag{4.7}$$

The values of the measured discharge probability are distributed over several orders of magnitude for any measurement. The capacitance of the THGEM and the cables connecting it to the picoammeter is 0.79 nF. Together with the 10 MΩ protection resistor this amounts to a dead time (5 RC) of $\sim$ 40 ms. Due to this dead time the discharge probability might be underestimated. Again, assuming the discharge occurrence undergoes a Poisson distribution one can determine the probability $P_{Poisson}$ of encountering a discharge within the 40 ms dead time t_{dead} at a rate r_{Dis} = 1 Hz and one obtains a probability below 0.1 % (equation 4.8). This is also the measure by what percentage the discharge probability might be underestimated due to the detector not being at full voltage,

$$P_{Poisson} = e^{-r_{\mathrm{Dis}} \cdot t_{\mathrm{dead}}} \sum_{k=2}^{k=\infty} \frac{(r_{\mathrm{Dis}} \cdot t_{\mathrm{dead}})^k}{k!} \,. \tag{4.8}$$

However, already at discharge rates above $\sim$0.25 Hz an extreme, non-exponential increase in the absolute gain can be observed. This effect is not yet fully understood and to avoid major corrections to the high-rate measurements, measurements are not continued at discharge rates larger than $\sim$0.25 Hz. With a source rate of $\sim$75 Hz this corresponds to discharge probabilities of $\sim 3.3 \cdot 10^{-3}$. In Fig. 4.10 a typical waveform of a primary discharge in a THGEM is pictured. The signal shows after an initial dip periodic oscillations which are caused by the inductance of the system.

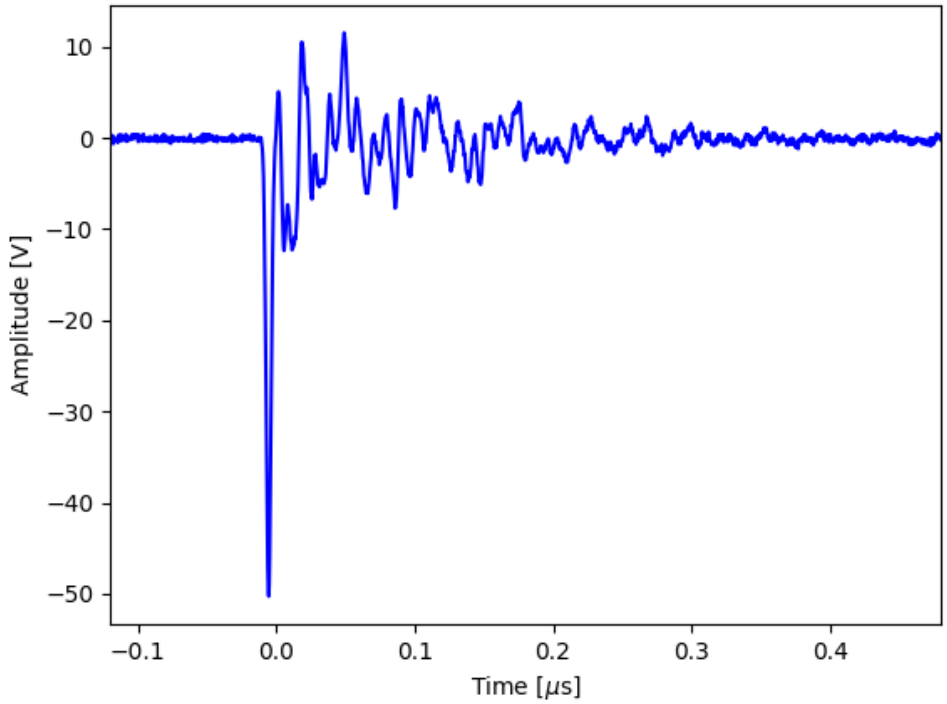

Figure 4.10: Oscilloscope signal of a primary discharge in a THGEM.

5 Simulation

A detailed simulation of the experimental setup has been developed to study the connection between discharge probability and charge density in a THGEM. The simulation framework is based on previous work for charge density studies in GEMs [57]. Similar studies also have been performed for Micromegas [9]. The simulation is performed with GEANT4 (Version 4.10.2.p02) [58] replicating the geometry of the detector setup described in chapter 4.1.

5.1 Model description

In the simulation heavily ionizing alpha particles are randomly emitted by a particle gun on the cathode. Energies and intensities of the alpha particles are modeled according to the experimental source described in table 4.1. The energy deposition of the alpha particles in the active medium is simulated in GEANT4. Every event embodies one single alpha particle and the simulation is performed on an event-by-event basis. The particle transport in GEANT4 is performed stepwise with interactions taking place after each step and under consideration of the 400 $\mathrm{V\,cm^{-1}}$ drift field. The distance between the steps is randomly sampled from the mean free path of the particle which is computed by taking into account the cross sections of physics processes summarised in the low-energy electromagnetic interaction physic list G4EmLivermorePhysics [59]. The distance between GEANT4 hits is smeared out according to a flat distribution. In GEANT4 at each hit the energy loss $\frac{dE}{dx}$ of the alpha particle in the medium is calculated via the well known Bethe-Bloch equation:

$$\frac{dE}{dx} = \frac{4\pi n e^4}{mc^2\beta^2} Z^2 \left(\log \frac{2mc^2\beta^2\gamma^2}{I} - \beta^2 \right) \tag{5.1}$$

where n is the electron density, mc^2 the energy of the electron, Z the charge of the travelling particle (in case of the alpha particle Z=2), β the ratio of velocity of the travelling particle to the speed of light and I the mean excitation energy of the atoms in the medium. I considers all relevant processes that can contribute to the energy deposit in the medium and that are contained in the physic list. The energy loss of a particle described by the Bethe-Bloch formula is inverse proportional to the square of their velocity due to the increase of the interaction cross section with decreasing particle energy. Thus a peak occurs shortly before the particle comes to a stop in the medium, the so-called Bragg peak. The energy loss as function of the track length for alpha particles of varying energy in different gases is shown in Fig. 5.1 [60]. The energy of the alpha particles in a)-c) is comparable to the energy of the alpha particles emitted by the isotopes of the mixed radioactive source used in the experimental setup. The large difference between mixtures containing Argon compared to mixtures containing Neon

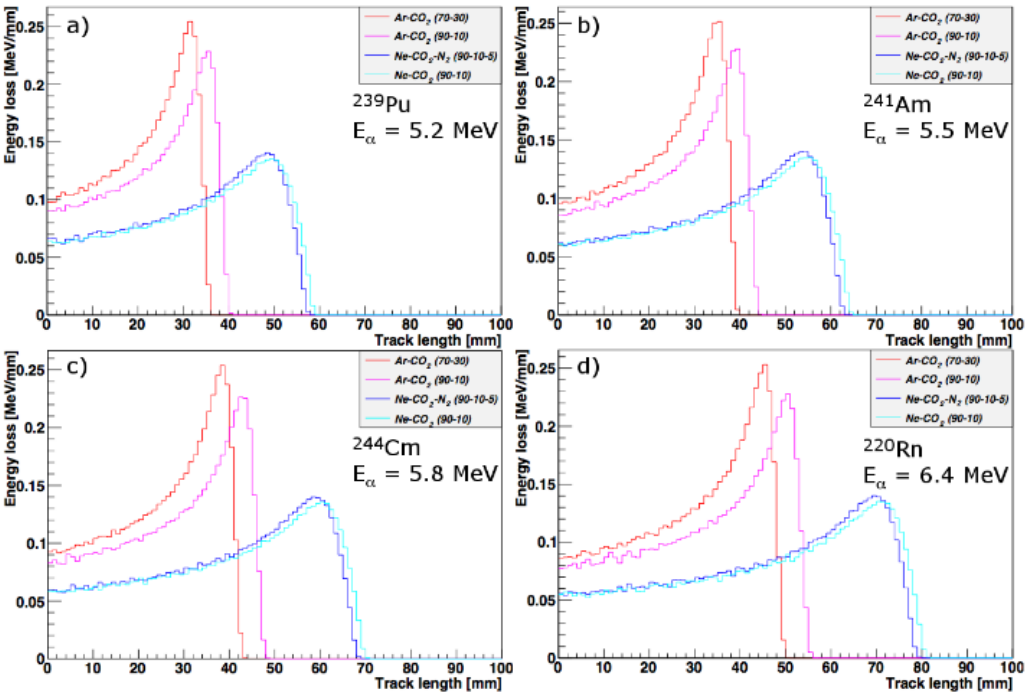

Figure 5.1: Bragg curves for alpha particles of different energies in different gas mixtures [60]. a)-c) correspond to the averaged alpha energies of the isotopes used in the radioactive source for this study.

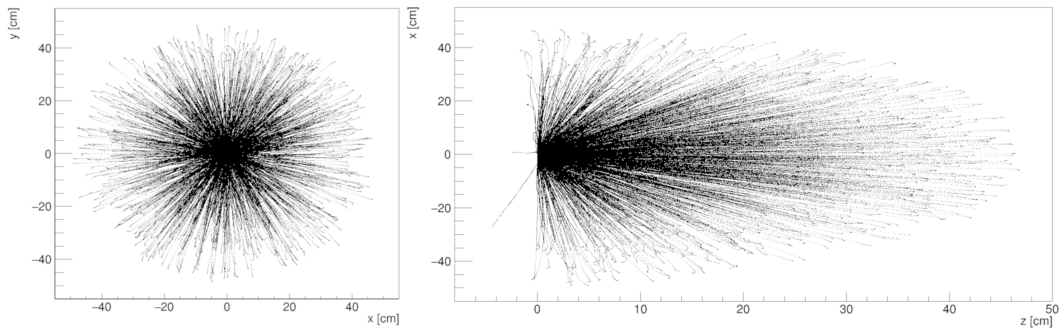

Figure 5.2: Simulated hits of 1000 alpha particles in Ar–CO_2 (90–10) in the y-x-plane (left) and x-z-plane (right). At the end of the tracks one can notice the increased interaction rate as the now low energetic particles get widely scattered.

can be explained by the density of these gases as the energy loss is directly proportional to the electron density which again is directly proportional to the medium density. The exact position and energy loss for each alpha hit is determined in GEANT4 and saved for further processing. In Fig. 5.2 simulated tracks of 1000 alpha events in Ar–CO_2 (90–10) can be seen. Every point corresponds to one hit of an alpha particle in the medium. Note the curl at the end of each track where the alpha particles lost most of their energy and get widely scattered. In the first analysis step the energy deposition at each hit $E_{\text{dep}}^{\text{hit}}$ is converted into primary electrons N_{primary} by using the effective ionisation potential W_i of the medium, see equation 5.2.

$$N_{\text{primary}} = \frac{E_{\text{dep}}^{\text{hit}}}{W_i} \tag{5.2}$$

Every primary electron is accelerated by the drift field and stopped in subsequent collisions with the medium. Due to its small mass compared to the gas atoms the electron momentarily loses direction after each collision but gets immediately reaccelerated towards the THGEM top electrode. The velocity picked up between collisions results in the macroscopic quantity of the drift velocity v_{drift}. The values for W_i, v_{drift} and other gas properties used in the simulations are computed in Magboltz and are listed in table 4.2 Through the collisions the electrons will thermalise and their energy distribution approaches the Maxwell-Boltzmann distribution. The direction of their movement is then uniformly distributed. Considering initially a point-like charge cloud that will spread with time resulting in a Gaussian distribution [61]:

$$n = \left(\frac{1}{\sqrt{4\pi Dt}}\right)^3 \exp\left(\frac{-r^2}{4Dt}\right) \tag{5.3}$$

Where D is the diffusion constant which depends on the electric and magnetic fields and the gas properties. In the case of this study no magnetic fields are present and just the electric drift field of $400\,\text{V}\,\text{cm}^{-1}$ plays a role. The width of the charge cloud σ reads then:

$$\sigma^2 = 2Dt \tag{5.4}$$

Given fixed gas properties and using t = $\frac{L}{v_{\text{drift}}}$ with drift length L being the distance that the electron has traveled one can write:

$$Dt = \frac{DL}{v_{\text{drift}}} \tag{5.5}$$

Therefore D can be redefined in order to calculate the electron spread directly from the drift length:

$$D^{'} = \sqrt{\frac{2D}{v_{\text{drift}}}} \tag{5.6}$$

Thus each electron is then diffused in three dimension according to a Gaussian distribution with a width of:

$$\sigma_{x,y,z} = D^{'}_{x,y,z}\sqrt{L_{x,y,z}} \tag{5.7}$$

However, electrons are differently experiencing the surrounding charge depending on their position in the charge cloud which gives rise to a spatial anisotropy in diffusion. Therefore a distinction between transverse and longitudinal diffusion is made. With the longitudinal diffusion (σ_z = D_L $\sqrt{\Delta z}$) taking effect in the direction parallel to the electric field and transverse diffusion in the directions perpendicular to the electric field ($\sigma_{x,y}$ = D_T $\sqrt{\Delta z}$).
As not all electrons from a single event arriving at the THGEM will contribute to a potential discharge only electrons arriving within a certain time frame will be considered. While a discharge itself happens on a very small timescale $\mathcal{O}$(ns) the exact timescale in which conditions contribute to the creation of a discharge is not known. Therefore the integration time t_{int} as a simulation parameter is introduced. All electrons within the distance d_{int} = $t_{\text{int}} \cdot v_{\text{drift}}$ above the THGEM are collected and then projected onto the THGEM plane. The position of the THGEM plane corresponds to the experimentally defined distances to the source d_{source} which is the sum of the drift gap (which is varied in the measurement) and the constant cathode thickness (1.5 mm).

After arriving at the THGEM plane the electrons get sorted into a hexagonal grid matching the distribution of the TGHEM holes. A schematic sketch of the simulation is pictured in Fig. 5.3. The single-electron response inside a THGEM hole follows, like in GEMs, a Polya distribution [62]. However, as in this study the number of electrons in a hole is large the central limit theorem can be applied and a symmetric Gaussian distribution can be assumed. Therefore it can be assumed that the formation of a discharge is only a consequence of the local concentration of charge inside a THGEM hole and one can relate the collected charges in a THGEM hole to a discharge probability. This is done in a second analysis step. The total charge inside a hole is then calculated by multiplying the collected primary electrons with an amplification factor or gain. The discharge probability then is the probability that a certain critical charge limit Q_{crit} is reached inside one THGEM hole for a given amplification and d_{source} and is normalized only by the total number of contributing events. Both the amplification and d_{source} is varied in this study. Only one discharge per simulated event and d_{source} may occur as after a spark the potential inside the THGEM holes breaks down and prevents the creation of further discharges, see also chapter 4.4. Due to the geometry of the THGEM not all simulated events may contribute to the discharge probability. Therefore, alpha particles with hits in or within 0.2 mm above the mounting hole or segment boundaries

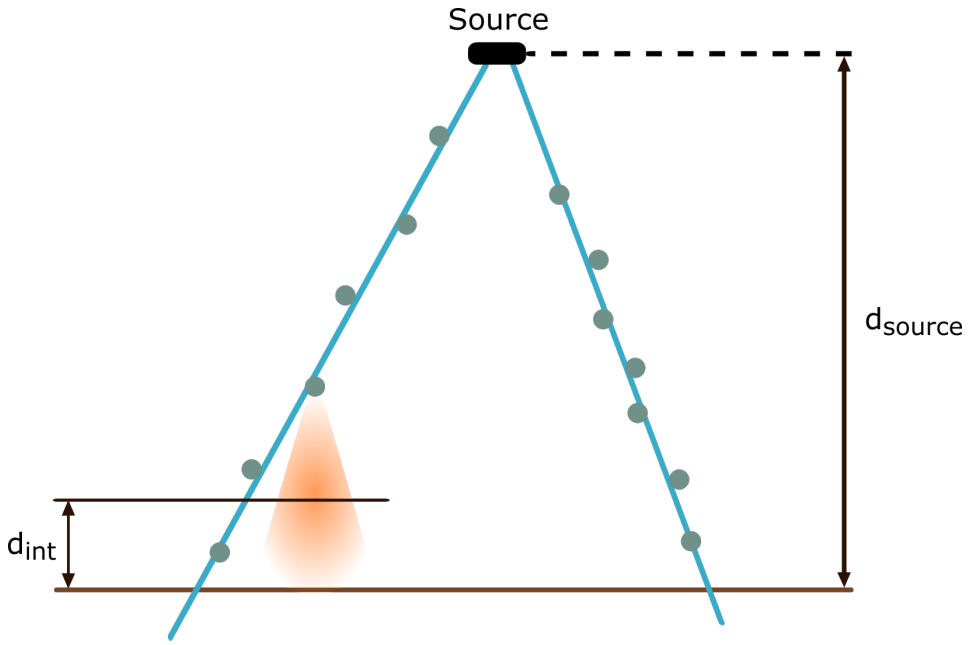

Figure 5.3: Schematic of the simulation. Alpha particles (blue line) are emitted by a source and deposit energy in the medium (grey dots). The created charges are then diffused (orange). Only electrons within d_{int} are considered for multiplication and are sorted into the honeycomb-like hole pattern of the THGEM which is placed a distance to source d_{source}.

d_{source} [mm]	Ne–CO_2 (90–10)	Ar–CO_2 (90–10)	Ar–CO_2 (70–30)
14.5	19810	18380	16550
24.5	9234	6507	5561
32.0	6133	2639	2773
37.0	5065	2010	1763
39.5	4196	1424	756
51.2	1612	0	0
59.5	472	0	0
71.0	1	0	0

Table 5.1: Number of alpha particles ending up in non-active regions of the THGEM for all gas mixtures and different d_{source} for a simulation with 10^6 events.

are not counted towards the normalization. See Fig. 4.3 for a photograph of the THGEM picturing the concerned non-active areas. In table 5.1 the number of alpha particles "lost" in the non-active THGEM area is listed for every gas and d_{source} for an exemplary simulation with 10^6 events; in all cases the correction to the total event count is below 2%. Electrons ending up in the non-active area of the THGEM after diffusion are also disregarded and this is done likewise for each d_{source}-plane.
After the initial simulation and the two analysis steps a discharge probability curve for every d_{source}, Q_{crit} and t_{int} as function of amplification factor as well as for every amplification factor a discharge probability curve as function of range is created.
In a third step the dependence of the model on the two free parameters Q_{crit} and t_{int} is studied by comparing the resulting discharge probability curves to the experimental data. The best values for the parameters is then found by χ^2 minimisation. The χ^2 is computed as follows:

$$\chi^2 = \sum_{i=1}^{n} \frac{(x_i - s_i)^2}{\sigma_i^2} \tag{5.8}$$

Where x_i is the value of the experimental discharge probability and s_i the discharge probability of the model and σ_i the uncertainty of the experimental discharge probability at point i. For the value of the model curve the curve is evaluated at the same position the experimental data lies. As the model curves are not continuous but sampled by a range of amplification values the curves are interpolated where no equivalent counterpart to the experimental data exist. The best fit is determined by the lowest reduced χ^2 value for every gas and d_{source}. The reduced χ^2 is the above calculated χ^2 divided by the number of degrees of freedom.

5.2 Software framework

The described model is a generalized version of the software used in the calculation of the critical charge density that leads to a discharge in GEMs [57]. Several changes were made to the version in the aforementioned paper. The geometry is not anymore fixed to a $10 \times 10\,\mathrm{cm}^2$ GEM but the side length of the studied GEM or GEM-like structure can now be

freely chosen. The software will be available online on GitHub [63]. The electric field above the GEM is made available as free parameter. The gas properties used in the simulation are now chosen automatically from external files according to the input gas mixture and electric field. Furthermore a plain modifier to the number of collected electrons is implemented naively mimicking the collection efficiency. The simulation is implemented in three stages in C++. Each stage processes the output of the previous one. An overview of the simulation workflow is shown in 5.4. The first stage contains the simulation of the alpha particles and their interaction with the gas in the detector. This is done in GEANT4.10.2.p02 using the G4EmLivermorePhysics physic list on an event-by-event basis for each alpha particle. The positions of each hit and the corresponding energy deposition is then used for further processing. Input arguments for this part are *gasFlag*, *EMfieldFlag* and *readoutSize*. The *readoutSize* stands for the side length of the THGEM in millimeter. The program always assumes a square geometry for the detector. The input parameter *gasFlag* is a integer number which corresponds to a certain gas mixture and selects with which gas the detector is filled. Currently gas properties for five different gas mixtures are available which are assigned numbers 0 through 4. With *EMfieldFlag* the drift field value in $\mathrm{V\,cm^{-1}}$ is set. The processing of the GEANT4 ouput is done with the data analysis framework ROOT 5.34/34 [64]. An overview of the components of this simulation step is listed below:

GEMsim.cc	Main file. Initializes and finalize all processes.
Detector.cc	defines detector geometry, materials and electric field. Takes *gasFlag*, *fieldFlag* and *readoutSize* as input.
PrimaryGeneratorAction.cc	defines the intensities and energies of the radioactive source according to table 4.1.
SensitiveDetector.cc	initalizes sensitive detector volume and collects information like energy deposited and position of alpha hits in the sensitive detector area. Also smears out the position between two hits.
WorldConstruction.cc	constructs large world volume containing the detector and its sensitive components.
InputHandler.cc	takes care of input parameters.
EventManager.cc	manages the initialization and end of each event.
RunManager.cc	initializes particle gun, physic list and world geometry and starts the simulation.
OutputManager.cc	creates and write output ROOT file. Also counts alpha particles hitting the non-active THGEM area (center hole, segment boundaries).
PhysicsList.cc	sets the physic list to G4EmLivermorePhysics.

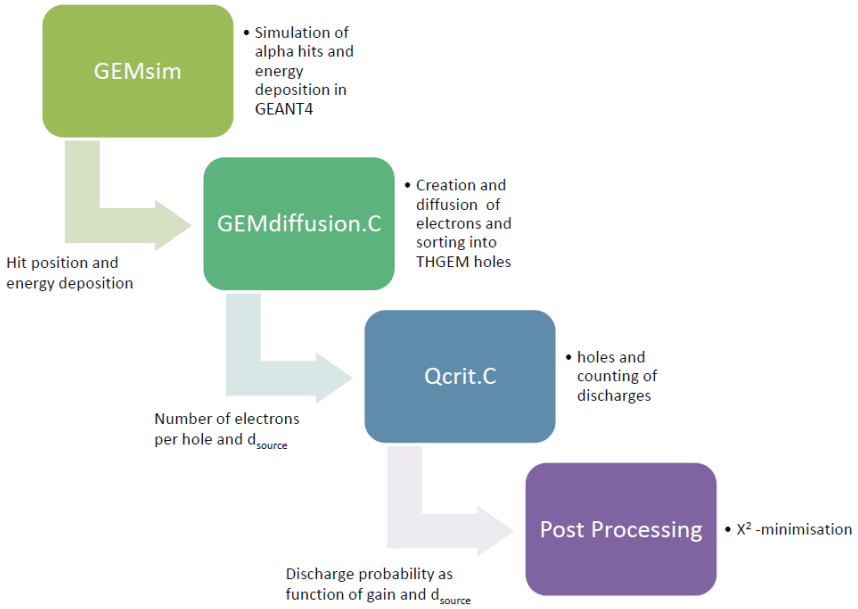

htbp

Figure 5.4: Workflow diagram of the software components.

StepMax.cc	sets the maximum step size to 1 mm.
GEMEvent.hpp	defines the GEMEvent and Hit class.

The class GEMEvent defined in GEMEvent.hpp is a ROOT TObject that stores the general information of the events: the number of hits, the energy deposition per event, the energies and ranges of the emitted alpha particles, an array of all hits in the detector and the number of alpha particles ending up in or 0.2 mm above the segment boundaries and the center hole of the THGEM for each d_{source}. Also defined in GEMEvent.hpp is the class Hit which stores the GEANT4 particle ID, the position and the deposited energy of each hit as well as the length between a hit and the previous hit. These objects created from this classes are saved in a ROOT file as a TTree at the end of this step.
The next stage processes the information about the alpha hits and computes the number of primary electrons created by the energy deposition of each hit as well as manages the diffusion of these electrons in the gas and their sorting. Input arguments are the aforementioned *gasFlag*, *readoutSize* and *EMfieldFlag* and in addition the integration time *tint*, the *pitch* between THGEM holes in µm, the number of simulated events *nEvents* and the *directory* where the ROOT file of the previous step resides. *EMfieldFlag*, *gasFlag* are used to select the right gas and gas properties. *nEvents* is the delimiter for the loop over all events. *Pitch* and *readoutSize* define the honeycomb-like grid of the TGHEM holes. All experimental values of d_{source} are considered in this step. Electrons which would end up on the non-active area of the THGEM after diffusion get dismissed and are not further processed. All the other electrons get collected

and sorted into the hexagonal grid of the THGEM. For the sorting the class GEM is created which assigns each electron to the proper THGEM hole also taking into account the shift between the hexagonal pads from one row to the next one. It uses *pitch*, *readoutSize* and x,y coordinates of the drifted electron as inputs. In order to save the output for further processing one object of class HitEvent and one of class HoleHit are created. The class HitEvent has the data members "mNhit", total number of hits in the detector,"mNevt" number of events and an array of hits in the detector mHits. The class HoleHit has the public data members "mZpos" containing d_{source} of electron matched to a specific hole and "mEle" which corresponds to the number of electrons in one single hole. HoleHit has also the member function "AddHit()" which sets the respective values of the data members for each hit. The last stage computes the discharge probability as function of gain and range for a combination of t_{Int} and Q_{crit} for every d_{source} respectively amplification factor. In addition to t_{Int} in ns and Q_{crit} it also takes a value for the collection efficiency *Ecoll* which is by default set to 1. Another input parameter is the file name of the output file of the last stage that is to be processed. *gasFlag*, *pitch*, *readoutSize* and *EMfieldFlag* need to be specified for creating a distinct output file name. A output directory can also be passed to the program otherwise the output will be written to the default directory. Lists of the multiplication factor and d_{source} steps are defined and looped over. For each event the number of electrons of every THGEM hole in which electrons got projected in the previous step is multiplied by an amplification factor. The resulting total charge is then compared with the Q_{crit} from the input. If it exceeds the critical charge a discharge is counted. This comparison is done for every multiplication factor in a predefined list and for every distance to source. For each event, distance to source and multiplication factor only one discharge can be caused. The discharge probability is then calcualted once as function of distance to source for every multiplication factor and once as function of multiplication factor for every distance to source.
The last stage is called for every t_{Int} and Q_{crit} that is listed in user defined external files. The final comparison of the simulated discharge curves to the experimental data and the extraction of the optimal values for t_{Int} and Q_{crit} by χ^2 minimization is done by ROOT scripts. The simulations are executed on a Linux batchfarm. Due to constraints in computation power the full statistic of stages one and two is split into several independent jobs that are later merged.

6 Results and discussion

6.1 Gain curves

For all measurements the absolute gain as function of the potential across the THGEM U_{THGEM} for all gas mixtures and distances to source is depicted in Fig. 6.1. The absolute gain is determined by the procedure described in section 4.3. The precision of the HV supply is sufficiently precise to neglect the uncertainties in U_{THGEM}. For the absolute gain the error bars are smaller or the same size as the symbols. No measurements where conducted for distances beyond the Bragg curve for the respective gases as no alpha particles which are necessary to reach the high charge density near the THGEM to trigger discharges would be able to reach the THGEM.

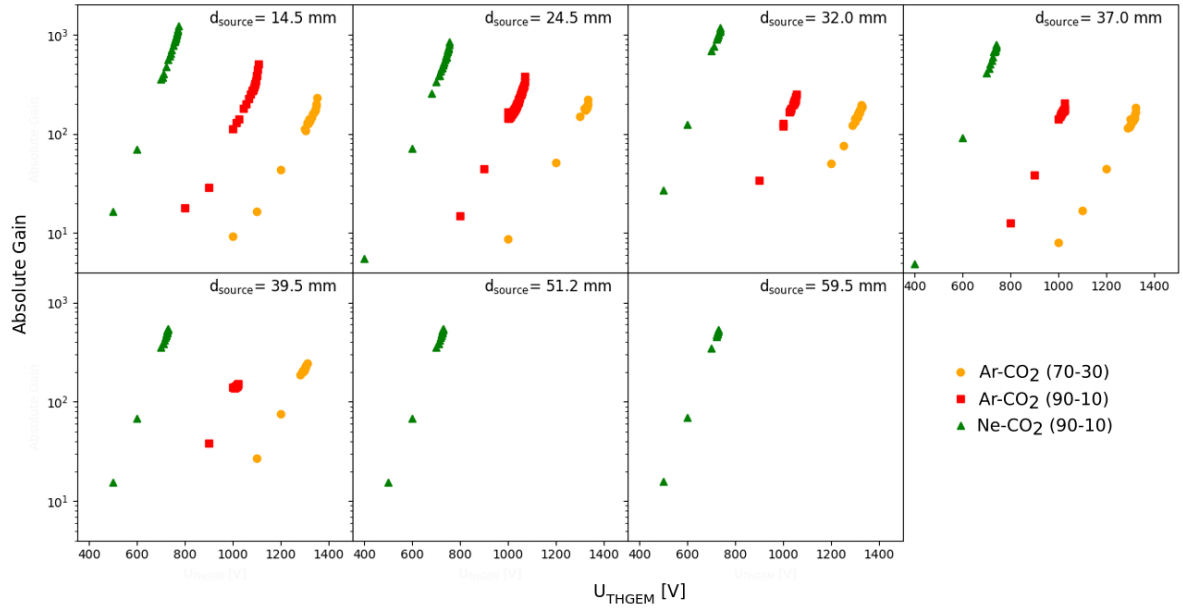

Figure 6.1: THGEM absolute gain as a function of the potential difference across the THGEM U_{THGEM} for every distance and all gas mixtures. The error bars are the same size or smaller than the symbols.

A hierarchy of gains between the gas mixtures can be recognised, as one would also expect in normal GEMs [65]. In Ne–CO_2 (90–10) higher gains then in the argon mixtures can be achieved due to the larger Townsend coefficient of neon. In the argon-based mixtures a larger admixture of quencher corresponds to lower gain for the same applied voltage. Over all

distances and gases the gain shows an exponential increase with applied voltage across the foil. However, at some point this trend is broken and the gain drops and rises again back to the trend level. In some cases with increasing voltage the gain even overshoots the trend level and increases further non-exponentially. The onset of this gain drop coincides with the first occurrence of discharges. Thus, this drop is likely correlated or might be even caused by discharge events in the THGEM. A possible change in the polarization of the PCB material could be hypothesized as explanation. However, the underlying mechanisms are not yet understood. The gains exhibit low variance over the drift length except for distances near the Bragg peak of the respective gases. At those distances the gain is slightly lower since the energy deposit of the particles and thus the amount of primary electrons entering the THGEM is larger. And with an increased number of charges entering the THGEM hole a lower gain is necessary to reach the critical charge limit for a spark.

6.2 Comparison of simulation to experimental data

The discharge probability as function of the THGEM absolute gain for different distances to the source d_{source} and for every gas is presented in Fig. 6.2. The discharge probability is measured for five different distances in Ar–CO_2 (70–30), four in Ar–CO_2 (90–10) and seven in Ne–CO_2 (90–10). d_{source} is the distance to source and is composed of the length of the drift gap which is varied and the 1.5 mm thick cathode PCB. The discharge probability in Ar–CO_2 (90–10) at d_{source} = 37 mm is very sensitive to slight gain changes due to the high local charge densities associated with the Bragg peak at this distance. This makes it experimentally difficult to measure a sufficiently distributed discharge probability curve as even the smallest possible change of U_{THGEM} (1 V) leads to large changes in absolute gain change. Therefore, measurements for Ar–CO_2 (90–10) at d_{source} = 37.0 mm are omitted.

As the maximum track length of alpha particles is about 2 cm larger in Ne–CO_2 (90–10) than in Ar-based mixtures two additional distances are measured only for Ne–CO_2 (90–10). It can be seen that the discharge probability strongly depends on the gas mixture. The differences are especially pronounced between the argon and the neon mixtures. For a given gain, the discharge probability in Ar–CO_2 (90–10) and Ar–CO_2 (70–30) is higher by several orders of magnitude than in Ne–CO_2 (90–10). This can be explained by basic features of the corresponding noble gas. The effective ionisation potential W_i is lower in argon-based mixtures than in neon, thus the the number of primary electrons liberated by the incident particle is higher. In addition, as mentioned above the range of alpha particles in the Ar-based mixture is almost 40 % shorter compared to the Ne-based. As a result, higher local charge densities are obtained in the Ar-based mixtures and it is more likely to exceed the critical charge limit. Thus, a higher discharge probability is observed.
Comparing the argon-based gas mixtures among themselves one gets a surprising result. Ar–CO_2 (90–10) seems to be more stable then Ar–CO_2 (70–30) for all d_{source} but 39.5 mm. However, at 39.5 mm the alphas are near their maximal energy deposit in Ar–CO_2 (90–10) whereas in Ar–CO_2 (70–30) most alphas are already stopped. This thus also fits into the picture. While not pictured, the onset of discharges starts also for 37.0 mm at lower gains in

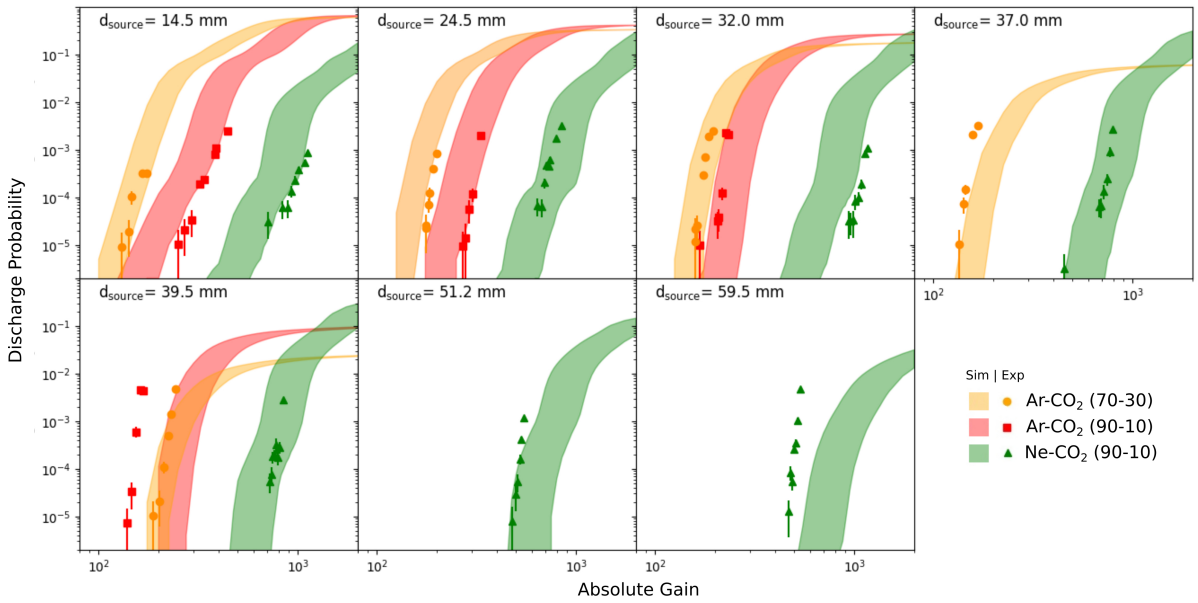

Figure 6.2: Discharge probability as a function of absolute gain. The bands indicate the simulation results, while the points correspond to measurements. The width of the simulation bands is related to the range of the values of the critical charge density. The integration time in the simulation is 50 ns for Ne–CO_2 (90–10), 40 ns for Ar–CO_2 (90–10) and 80 ns for Ar–CO_2 (70–30).

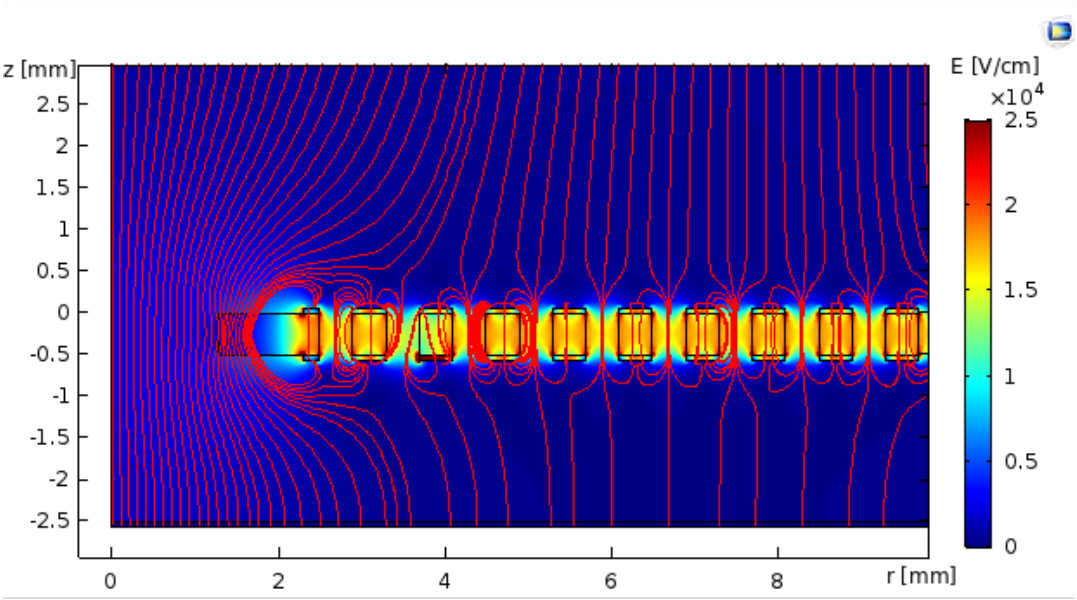

Figure 6.3: COMSOL simulation of the electric fields in vicinity of the TGHEM. The THGEM cross section shows (from right to left): the center mounting hole, nine individual THGEM holes and a segment boundary. Red streamlines and colored contour illustrate the electric field strength.

Ar–CO_2 (70–30) than in Ar–CO_2 (90–10). One would expect the opposite as Ar–CO_2 (70–30) contains a larger admixture of quencher. The quencher gas is commonly used to increase the stability of detectors. CO_2 as quencher can absorb UV photons created by the amplification processes through its rotational and vibrational levels and its lower ionization energy also allows to exchange charge with the noble gas ions. Thus, a higher quencher admixture should lower the discharge probability. The measurement setup was thoroughly investigated for any possible problems but none have been found. However, this inversion of stability could be explained by the very specific geometry of the THGEM used in this setup and its resulting electric field. The THGEM has a 4.6 mm large mounting hole in its center creating a non-active area right below the radioactive source. Due to the center hole incoming charges from the drift gap might not experience a homogeneous drift field of 400 V cm^{-1} defined by the potential at the cathode and THGEM top electrode. The electric field around the center hole is instead defined by the potential between cathode and anode leading to an enhanced drift field in its vicinity. To investigate this effect a simulation in COMSOL Multiphysics 5.2. [66] is conducted. COMSOL is a multiphysics simulation software solving problems with finite element methods. A 2D axisymmetric section of the THGEM with dimensions matching the real THGEM is created. The drift gap is 14.5 mm and the induction gap 2 mm. The origin of the is the center mounting hole. The simulation is carried out in realistic conditions with a drift field of 400 V cm^{-1} and a potential across the THGEM of 1000 V and no field below the THGEM. The results of the simulation can be seen in Fig. 6.3. The red streamlines indicate that the field around the center hole is greatly increased and also affects up to four

surrounding rows of THGEM holes. Electric fields of up to $5\,\mathrm{kV\,cm^{-1}}$ are found inside the center hole. Primary electrons which would normally enter one of the THGEM holes close by are sucked into the center hole and are lost for amplification and thus can not contribute to the formation of discharges.

An interaction between the different gas properties modified by the enhanced electric fields especially near the center hole might be able to explain the observed inversion in the stability hierarchy. For a conclusive approach a full simulation of the electric field configuration for this specific geometry would be necessary.

Nonetheless, a simulation only considering the real geometric size of the center hole has been conducted and the best fit to the measurements has been determined by χ^2-minimisation as described in section 5.1. The amplification factor has been varied between 25 and 1000 in steps of 25, between 1000 and 1500 in steps of 50 and from 1500 to 2000 in steps of 250. The free parameter t_{int} was varied in the range from 2 ns to 120 ns. As unphysical values of t_{int} for Ar–CO_2 (90–10) at d_{source} = 14.5 mm and Ne–CO_2 (90–10) at d_{source} = 24.5 mm yield the lowest χ^2 t_{int} was constrained to values between 10 and 120 ns. The other free parameter Q_{crit} is varied between 5×10^5 and 16×10^6. For Q_{crit} below 1×10^6 and above 10×10^6 the step size is 5×10^5, 1×10^5 otherwise it is 1×10^5.

The quality of the fit is summarized by means of a reduced χ^2-map for the two free parameter t_{int} and Q_{crit} for each gas and distance to source. In Fig. 6.4 an exemplary reduced χ^2-map for Ne–CO_2 (90–10) and d_{source} = 37 mm is shown. The lowest value of the reduced χ^2 determines the best fit. The number of degrees of freedom corresponds to the number of measurement points. The lowest value of χ^2 and the according values of t_{int} and Q_{crit} for each individual combination of gas and distance to source are listed in Table 6.1. For Ne–CO_2 (90–10) the lowest values of χ^2 are achieved for t_{int} between 20 and 110 ns and Q_{crit} between 3.6×10^6 and 7.8×10^6, in Ar–CO_2 (90–10) for t_{int} between 15 and 60 ns and Q_{crit} between 2.8×10^6 and $4.4\times10^6$and in Ar–CO_2 (70–30) for t_{int} between 80 and 120 ns and Q_{crit} between 2.0×10^6 and 2.8×10^6. The best value for t_{int} are then 50 ns for Ne–CO_2 (90–10), 40 ns for Ar–CO_2 (90–10) and 80 ns for Ar–CO_2 (70–30). The best χ^2 for the respective t_{int} values defines the range from which the final Q_{crit} is calculated for each gas. In Ne–CO_2 (90–10) Q_{crit} varies between 3.6×10^6 and 7.8×10^6, in Ar–CO_2 (90–10) between 2.2×10^6 and 4.4×10^6 and in Ar–CO_2 (70–30) between 1.6×10^6 and 2.4×10^6 The final critical charge limit can then be determined for each gas by the RMS and the uncertainties are given by its root mean square deviation. One gets the in Table 6.2 presented values. The uncertainty of the Q_{crit} values is then related to the width of the simulation band. The width of the simulation bands accommodate the uncertainty of the Q_{crit} values. The simulation outcome is generally in good agreement with the measurements and also describes the stability inversion of Ar–CO_2 (70–30) and Ar–CO_2 (90–10) reasonably well. The largest deviation between measurements and simulation exist for d_{source} = 59.5 mm in Ne–CO_2 (90–10), for d_{source} = 39.5 mm in Ar–CO_2 (90–10) and in Ar–CO_2 (70–30) for d_{source} = 37.0 mm. The discharge probability is in these cases overestimated by the simulation. This might be due to the field distortion by the center hole as discussed above. Since these distances correspond approximately to the maximum track length of alphas in the respective gases and considering that the source is mounted directly above the center

hole most of the alphas being able to reach the THGEM are emitted perpendicularly from the source. Therefore, at these distances a particularly large amount of primary electrons are created close to the center hole and might get lost for the amplification and potential discharges.
The resulting values for the critical charge differ between the gases and are for all gases in agreement with the Raether limit. The magnitude of the critical charge limit of each gas compares well to the experimental results. The larger Q_{crit} the less discharge probability for a given absolute gain and the more stable the gas mixture. And indeed the most stable gas mixture, Ne–CO_2 (90–10), has a larger critical charge than the less stable Ar-based mixtures and the in the measurement more stable Ar–CO_2 (90–10) has similarly a higher Q_{crit} than Ar–CO_2 (70–30). The especially low critical charge and the high integration time in Ar–CO_2 (70–30) is coherent with the slow drift velocity in this gas. As the electrons drift slowly the time until the critical charge is reached has to be increased. While in Ar–CO_2 (70–30) the amount of quencher increases the stability of the THGEM, the shorter alpha range and lower effective ionisation potential compared to Ar–CO_2 (90–10) decreases the stability and one would expect similar charge densities. The difference in Q_{crit} then can be explained by the different transport properties distributing the primary ionisation differently. The gas properties might deviate from the ones listed in Table 4.2 as the particular THGEM geometry used in this study modifies the electric field close to the center hole and thus also the gas properties in this region. The integration time t_{int} has been introduced to the model as parameter to describe the charge accumulation. The integration time in Ar-based mixtures seems to scale with the drift velocity. In Ar–CO_2 (70–30) the t_{int} of 80 ns is two times larger than in Ar–CO_2 (90–10) with t_{int} of 40 ns, while the drift velocity is about three times smaller. It has been suggested for GEMs that for integration times larger than the transfer time of electrons which are in the order of ns additional mechanisms beyond the simple collection of charge is expected [8]. For THGEMs a similar argument can be made even if the transfer time of electrons is not known however the in t_{int} subsumed mechanisms would likely also have to scale with the drift velocity. Similar should be true for GEMs. An integration time of several ns is consistent with the streamer model which requires an existing space charge that modifies the amplification field [4].

The discharge probability as function of the drift length is shown in Fig. 6.5 for Ne–CO_2 (90–10) with an integration time of 50 ns and a simulated gain of 700, in Fig. 6.6 for Ar–CO_2 (90–10) with an integration time of 40 ns and a simulated gain of 250 and in Fig. 6.7 for Ar–CO_2 (70–30) with an integration time of 80 ns and a simulated gain of 200. Since there is no single gain value for which the discharge probability is measured at all distances and an interpolation of the experimental gain due to its non-exponential behavior is not possible, measured gain values that lie sufficiently close to each other and the simulated gain ($\pm$ 10%) are taken instead. Uncertainties based on this selection are not considered in the figures. For the two largest distances in Ne–CO_2 (90–10) and Ar–CO_2 (90–10) and the second largest distance in Ar–CO_2 (70–30) a larger discrepancy to the simulated gain is accepted as there are no measurements near the chosen gain. The concerned gain values are then $\sim$540 for the neon mixture respectively $\sim$170 for the argon mixtures. For all gases an increase of discharge

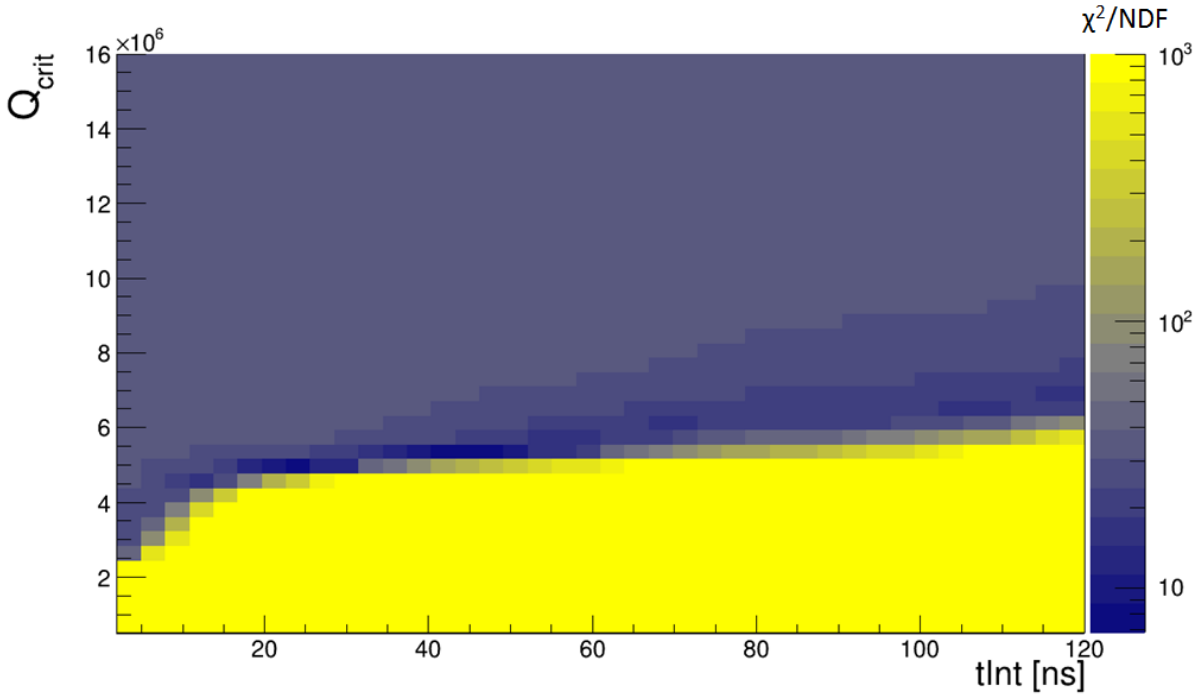

Figure 6.4: χ^2-map of Ne–CO_2 (90–10) at d_{source} = 37 mm for the two free mode parameters t_{int} and Q_{crit}. On the right the contour scale for the reduced χ^2.

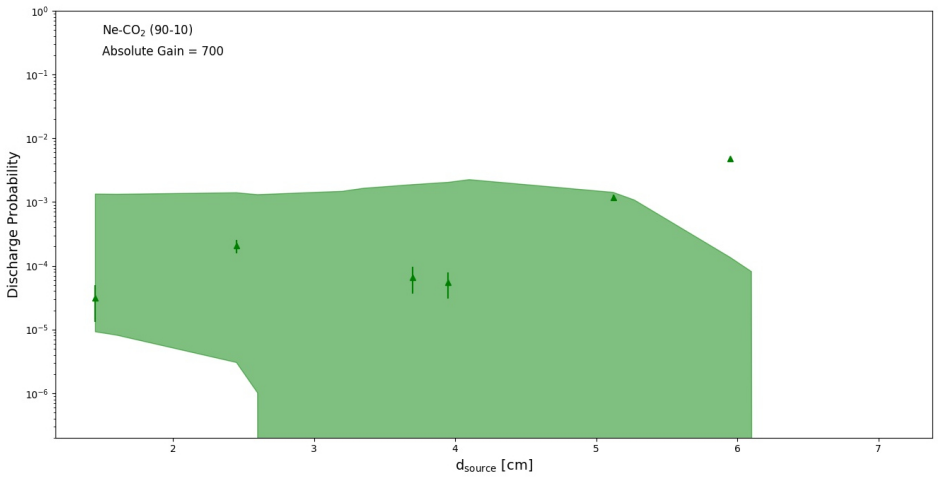

Figure 6.5: Discharge probability as a function of the distance to source for Ne–CO_2 (90–10). The result of the simulation for a fixed absolute gain of 700 is indicated by the band. The measurement points correspond to a similar absolute gain except for the two largest distances which correspond to a gain of $\sim$540. The integration time in this simulation is 50 ns.

	d_{source} [mm]	χ^2/NDF	t_{int} [ns]	Q_{crit} [$\times 10^6$]
Ne–CO_2 (90–10)	14.5	2.17304	50	7.6
	24.5	4.55109	20	4.8
	32.0	1.26875	48	7.8
	37.0	1.0121	40	5.2
	39.5	5.0523	40	5.6
	51.2	3.4517	35	3.6
	59.5	19.7315	110	6.1
Ar–CO_2 (90–10)	14.5	3.89814	40	4.4
	24.5	4.52758	15	3.0
	32.0	35.4872	40	3.1
	39.5	21.612	60	2.8
Ar–CO_2 (70–30)	14.5	1.66522	80	2.2
	24.5	4.13215	110	2.8
	32.0	9.58416	120	2.6
	37.0	43.9382	110	2.0
	39.5	42.4409	120	2.6

Table 6.1: Overview of best reduced χ^2 values and their associated Q_{crit} and t_{int} values each distance and gas mixture.

Gas	Q_{crit}
Ne–CO_2 (90–10)	$(5.9 \pm 1.4) \times 10^6$
Ar–CO_2 (90–10)	$(3.5 \pm 0.7) \times 10^6$
Ar–CO_2 (70–30)	$(2.0 \pm 0.3) \times 10^6$

Table 6.2: Values of critical charge Q_{crit} for different gas mixtures and an integration time t_{int} of 50 ns for Ne–CO_2 (90–10), 40 ns for Ar–CO_2 (90–10) and 80 ns for Ar–CO_2 (70–30).

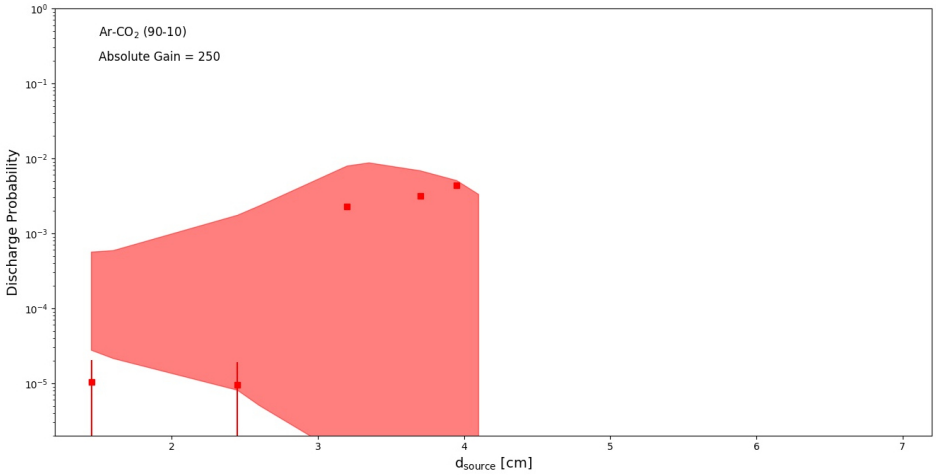

Figure 6.6: Discharge probability as a function of the distance to source for Ar–CO_2 (90–10). The result of the simulation for a fixed absolute gain of 250 is indicated by the band. The measurement points correspond to a similar absolute gain except for the two largest distances which correspond to a gain of ~ 170. The integration time in this simulation is 40 ns.

probability with distance is observed at first. The discharge probability then suddenly drops over several orders of magnitude at distances around 4 cm in the mixtures containing argon and around 6 cm in Ne–CO_2 (90–10).
This behavior is expected as the discharge probability is enhanced when alpha particles pass through THGEM holes or are stopped in their vicinity since then the highest local primary charge densities in single holes occur. The local energy deposition of an alpha particle is the highest towards the end of its trajectory which leads to a strong increase of the discharge probability at distances shortly before the particle comes to rest. At some distance the drift length is so large that the alphas can no longer reach the THGEM and the discharge probability drops severely. The primary ionisation will still reach the THGEM due to the charge transport in the drift volume however, the resulting charge density is then already to a great extent diluted by diffusion such that the probability to create a discharge is notably lower. It is noticeable that the simulated range curves for Ar–CO_2 (90–10) and Ne–CO_2 (90–10) have very broad simulation bands even though gain and t_{int} are fixed. This might be explained by the fact that these gases have a significantly lower t_{int} compared to Ar–CO_2 (70–30) and that d_{source} can be related to the primary charge densities. Since t_{int} determines the charge accumulation it is less likely to exceed a certain Q_{crit} for low values of t_{int}. As the upper limit for Q_{crit} determines the lower bound of the simulation band broadened towards shorter d_{source}. In future studies it might be possible to constrain the upper limit of Q_{crit} due to this consideration. As a result of the emission of the particles within a solid angle element defined by the finite source dimensions and the hole in the cathode PCB it is not possible to relate the measured points directly to the Bragg curve. Thus, a simulation considering the detector geometry and computing the local energy deposit as presented above is necessary.

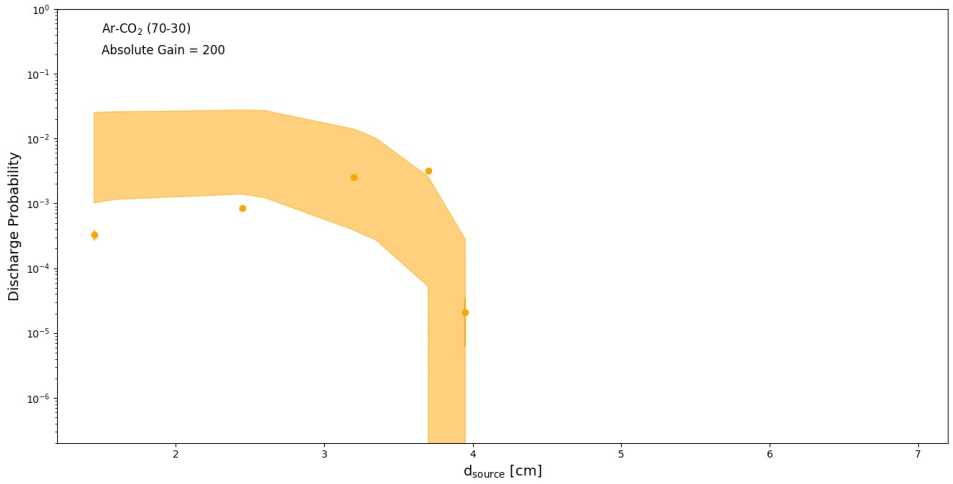

Figure 6.7: Discharge probability as a function of the distance to source for Ar–CO_2 (70–30). The result of the simulation for a fixed absolute gain of 200 is indicated by the band. The measurement points correspond to a similar absolute gain except for the second largest distance which corresponds to a gain of ~ 170. The integration time in this simulation is 80 ns.

Summarising, one can conclude that the charge density inside a THGEM hole is the driving factor behind the discharge formation in THGEMs and that the amount of drifted primary charges reaching the detector has less influence. The values for the critical charge Q_{crit} differ between the gases and can explain the measurements. The different values of t_{int} and Q_{crit} for different gases might enable the investigation of the underlying mechanisms of discharge formation in different media.

Gas	GEM Q_{crit} [x10^6]	THGEM Q_{crit} [x10^6]
Ar–CO_2 (90–10)	4.7 ± 0.6	3.5 ± 0.7
Ne–CO_2 (90–10)	7.3 ± 0.9	5.9 ± 1.4

Table 6.3: Values of the critical charge Q_{crit} for different gas mixtures for GEM and THGEM. The integration time t_{int} is 40 ns for Ar–CO_2 (90–10) in case of the THGEM and 30 ns in case of the GEM. For Ne–CO_2 (90–10) a t_{int} of 50 ns for the THGEM as well as for the GEM is used.

6.3 Comparison of GEM and THGEM

The obtained values for the integration time t_{int} and the critical charge Q_{crit} for different gases in a THGEM can be compared to those obtained with the same framework for a standard $10 \times 10\,cm^2$ GEM [8].
In Table 6.3 the values of Q_{crit} for GEM and THGEM in Ar–CO_2 (90–10) and Ne–CO_2 (90–10) are presented. A Q_{crit} for Ar–CO_2 (70–30) in GEMs is reported but was only obtained for a single distance which is not sufficient for a useful comparison. A t_{int} of 30 ns for Ar–CO_2 (90–10) and 50 ns for Ne–CO_2 (90–10) in the GEM match well with the for the THGEM obtained 40 ns for Ar–CO_2 (90–10) and likewise 50 ns for Ne–CO_2 (90–10).

The critical charge limits of the respective gases for GEM and THGEM agree with each other within their uncertainties and are consistent with the Raether limit. In both detector technologies Ne–CO_2 (90–10) has a higher critical charge than Ar–CO_2 (90–10) showing that the effect of the gas mixture on the Q_{crit} is more pronounced than the design difference of THGEM and GEM. Within uncertainties there is even no significant difference between GEM and THGEM regarding critical charge limit Q_{crit} and integration time t_{int}.
Given the dimensions of the THGEM in Section 4.1 the volume of a single THGEM hole can be determined to be $0.236\,mm^3$. With the volume the critical charge per THGEM hole Q_{crit} can be converted to a specific charge density. The same can be done for the GEM. A standard GEM with a thickness of 50 µm and a outer hole radius of the conical hole of 70 µm and an inner radius of 50 µm has a hole volume of $0.00057\,mm^3$. Therefore, the specific charge density necessary to trigger a discharge in a single THGEM hole and a single GEM hole can be given for each gas. In the THGEM the Q_{crit} of Ar–CO_2 (90–10) corresponds to a specific charge density of $(2.37 \pm 0.47)\,pC\,mm^{-3}$ and in Ne–CO_2 (90–10) to to a specific charge density of $(4.00 \pm 0.94)\,pC\,mm^{-3}$. In the GEM the respective specific charge densities in the hole are $(1.32 \pm 0.17)\,nC\,mm^{-3}$ in Ar–CO_2 (90–10) and $(2.05 \pm 0.25)\,nC\,mm^{-3}$ in Ne–CO_2 (90–10). The difference of three orders of magnitude in the specific charge density between GEM and THGEM is for similar values of Q_{crit} expected due to the disparity in size.
Not only is the charge per mm^3 lower in the THGEM, also the critical charge is systematically lower in THGEM even though it coincides within the uncertainties for THGEM and GEM. It can be hypothesized that more pre-accumulated charge inside the holes could compensate for the slightly lower critical charge value in the larger hole volume of the THGEM. While this charge could be correlated to the charge-up, charge-up alone can not be responsible

for the large difference in specific charge density. The total number of charges, which pass through the THGEM holes during the charge-up is only in the order of 100 pC for the whole THGEM [38].

7 Conclusion and outlook

This thesis presents the results of systematic studies of the discharge probability in a single THGEM detector exposed to an alpha source in Ar–CO_2 (90–10), Ar–CO_2 (70–30) and Ne–CO_2 (90–10). Gain and discharge probability have been measured for different distances to the alpha source in the three gas mixtures. For this a procedure to determine the absolute gain considering the charge-up of the THGEM and distortions due to discharges has been developed. A non-exponential behavior of the absolute gain in the discharge region is observed. A previously existing simulation framework used for discharge probability studies in GEMs has been generalized and applied to THGEMs. In the GEANT4 simulations a detector was exposed to highly ionizing alpha particles replicating precisely the measurement setup. In the Monte Carlo simulation the energy deposit and created primary electrons at each hit of an alpha track in the detector medium is calculated. The so created primary ionisation distribution is then diffused towards the THGEM plane taking into account basic gas properties. The THGEM plane is placed at different distances to the source mirroring the experimental setup. The at the plane collected electrons are then sorted into the holes of the THGEM. By comparing the simulation with the measurement a critical charge Q_{crit} is determined. If Q_{crit} is exceeded in a single hole a discharge occurs. Thus, a discharge probability is computed by normalising the number of events in which Q_{crit} is exceeded with the number of emitted alpha particles reaching the active area of the detector. The measured discharge probability curve could be reproduced with the simulations and the critical charge for each gas could be determined. A critical charge per THGEM hole of $(5.9 \pm 1.4) \times 10^6$ for Ne–CO_2 (90–10), $(5.9 \pm 1.4) \times 10^6$ for Ar–CO_2 (90–10) and $(3.5 \pm 0.7) \times 10^6$ for Ar–CO_2 (70–30) $(2.0 \pm 0.3) \times 10^6$ is obtained. The resulting values for Q_{crit} are in line with the predictions based on the Raether limit. It can be therefore concluded that charge density is a driving factor behind discharge formation in THGEMs. The presented values for the critical charge allow to estimate discharge rates in future THGEM-based detectors for a given primary charge distribution. Simulation results for the discharge probability as function of the distance to source are also presented. And it is shown that the discharge probability in Ne–CO_2 (90–10) is lower than in Ar-based mixtures due to the higher ionisation potential and larger alpha range. For Ar–CO_2 (70–30) and Ar–CO_2 (90–10) an inversion in the expected discharge probability behavior has been found. Even though Ar–CO_2 (70–30) contains more quencher is it less stable than Ar–CO_2 (90–10). This is found both in measurement and simulation. The reason for this may lie in the specific geometry of the THGEM which has in the center a mounting hole which creates a dead area and modifies the electric field as incoming charges may see the anode potential. This assumption is shows to be true in the light of a conducted COMSOL simulation showing the enhanced field around the center hole that also influences surrounding THGEM holes. Future plans include a complete field map

simulation of the detector that could be implemented into the simualtion framework. The obtained critical charge value for the THGEM in Ar–CO_2 (90–10) and Ne–CO_2 (90–10) is compared to previous results in GEMs in the same gases which were obtained by the same base framework. The THGEM values for Q_{crit} coincides within uncertainties with the Q_{crit} values of the GEM for each individual gas mixture. This shows that gas properties are more important for the discharge formation then detector technology. Furthermore, the charge density per volume for GEM and THGEM has been calculated. It is on the order of $pC\,mm^{-3}$ for the THGEM and $nC\,mm^{-3}$ for the GEM. It is planned for the future to make the charge density simulation framework available to the public.

Acknowledgments

I would like to thank everyone who helped and supported me throughout this thesis. First of all, i wish to thank Piotr Gasik for his supervision, his time, patience and advice. Furthermore, Prof. Laura Fabbietti for the privilege to work in her group. And on that note i also wish to thank the whole E62 group for the pleasant atmosphere every single one helps to create everyday. I also would like to thank Andreas Mathis for his help setting up the simulation and during the early days. A big thank you also goes to Thomas Klemenz for his general help and support regarding everything and, of course, his valuable comments on anything written. The GEM Crew would not be the GEM Crew without Berkin Ulukutlu. I thank him for his company in the laboratory, interesting and inspiring discussions and comments on this thesis. Due thanks also to Tobias Waldmann for his help and company in the GEM Lab. And not to forget the usual suspects for the usual things.
And finally, Chilo Garabatos from GSI Darmstadt for providing the Magboltz data for the gas properties used in the simulation.

List of Figures

List of Tables

Bibliography

[1] R. Chechik et al. "Thick GEM-like hole multipliers: properties and possible applications". In: *Nuclear Instruments and Methods in Physics Research Section A: Accelerators, Spectrometers, Detectors and Associated Equipment* 535.1 (2004). Proceedings of the 10th International Vienna Conference on Instrumentation, pp. 303 –308. DOI: https://doi.org/10.1016/j.nima.2004.07.138. URL: http://www.sciencedirect.com/science/article/pii/S0168900204016663.

[2] R. Chechik, A. Breskin, and C. Shalem. "Thick GEM-like multipliers—a simple solution for large area UV-RICH detectors". In: *Nuclear Instruments and Methods in Physics Research Section A: Accelerators, Spectrometers, Detectors and Associated Equipment* 553.1-2 (2005), 35–40. ISSN: 0168-9002. DOI: 10.1016/j.nima.2005.08.003. URL: http://dx.doi.org/10.1016/j.nima.2005.08.003.

[3] F. Sauli. "GEM: A new concept for electron amplification in gas detectors". In: *Nuclear Instruments and Methods in Physics Research Section A: Accelerators, Spectrometers, Detectors and Associated Equipment* 386.2 (1997), pp. 531 –534. ISSN: 0168-9002. DOI: https://doi.org/10.1016/S0168-9002(96)01172-2. URL: http://www.sciencedirect.com/science/article/pii/S0168900296011722.

[4] S. Franchino et al. "Effects of high charge densities in multi-GEM detectors". In: *2015 IEEE Nuclear Science Symposium and Medical Imaging Conference (NSS/MIC)* (2015). DOI: 10.1109/nssmic.2015.7581778. URL: http://dx.doi.org/10.1109/NSSMIC.2015.7581778.

[5] H. Raether. *Electron avalanches and breakdown in gases*. Butterworths, 1964.

[6] A Bressan et al. "High rate behavior and discharge limits in micro-pattern detectors". In: *Nuclear Instruments and Methods in Physics Research Section A: Accelerators, Spectrometers, Detectors and Associated Equipment* 424.2 (1999), pp. 321 –342. ISSN: 0168-9002. DOI: https://doi.org/10.1016/S0168-9002(98)01317-5. URL: http://www.sciencedirect.com/science/article/pii/S0168900298013175.

[7] V. Peskov et al. "The study and optimization of new micropattern gaseous detectors for high-rate applications". In: *IEEE Transactions on Nuclear Science* 48.4 (2001), pp. 1070–1074. DOI: 10.1109/23.958725.

[8] P. Gasik et al. "Charge density as a driving factor of discharge formation in GEM-based detectors". In: *Nucl. Instrum. Meth.* A870 (2017), pp. 116–122. DOI: 10.1016/j.nima.2017.07.042. arXiv: 1704.01329 [physics.ins-det].

[9] S. Procureur et al. "A Geant4-based study on the origin of the sparks in a Micromegas detector and estimate of the spark probability with hadron beams". In: *Nuclear Instruments and Methods in Physics Research Section A: Accelerators, Spectrometers, Detectors and Associated Equipment* 621.1 (2010), pp. 177 –183. ISSN: 0168-9002. DOI: https://doi.org/10.1016/j.nima.2010.05.024. URL: http://www.sciencedirect.com/science/article/pii/S0168900210011216.

[10] G. Charpak et al. "The use of multiwire proportional counters to select and localize charged particles". In: *Nuclear Instruments and Methods* 62.3 (1968), pp. 262 –268. ISSN: 0029-554X. DOI: https://doi.org/10.1016/0029-554X(68)90371-6. URL: http://www.sciencedirect.com/science/article/pii/0029554X68903716.

[11] A. Oed. "Position-sensitive detector with microstrip anode for electron multiplication with gases". In: *Nuclear Instruments and Methods in Physics Research Section A: Accelerators, Spectrometers, Detectors and Associated Equipment* 263.2 (1988), pp. 351 –359. ISSN: 0168-9002. DOI: https://doi.org/10.1016/0168-9002(88)90970-9. URL: http://www.sciencedirect.com/science/article/pii/0168900288909709.

[12] R. Chechik et al. *Thick GEM-like (THGEM) detectors and their possible applications*. 2006. arXiv: physics/0606162 [physics.ins-det].

[13] A. Breskin et al. "A concise review on THGEM detectors". In: *Nuclear Instruments and Methods in Physics Research Section A: Accelerators, Spectrometers, Detectors and Associated Equipment* 598.1 (2009). Instrumentation for Collding Beam Physics, pp. 107 –111. ISSN: 0168-9002. DOI: https://doi.org/10.1016/j.nima.2008.08.062. URL: http://www.sciencedirect.com/science/article/pii/S0168900208012047.

[14] M. Alexeev et al. "Micropattern gaseous photon detectors for Cherenkov imaging counters". In: *2008 IEEE Nuclear Science Symposium Conference Record*. 2008, pp. 1335–1340. DOI: 10.1109/NSSMIC.2008.4774663.

[15] A. Breskin et al. "The THGEM: A thick robust gaseous electron multiplier for radiation detectors". In: *Nuclear Instruments and Methods in Physics Research Section A: Accelerators, Spectrometers, Detectors and Associated Equipment* 623.1 (2010). 1st International Conference on Technology and Instrumentation in Particle Physics, pp. 132 –134. ISSN: 0168-9002. DOI: https://doi.org/10.1016/j.nima.2010.02.172. URL: http://www.sciencedirect.com/science/article/pii/S0168900210004390.

[16] M. Alexeev et al. "The gain in Thick GEM multipliers and its time-evolution". In: *JINST* 10.03 (2015), P03026. DOI: 10.1088/1748-0221/10/03/P03026.

[17] M. Baruzzo et al. "Direct measurements of the properties of Thick-GEM reflective photocathodes". In: (2019). arXiv: 1910.05257 [physics.ins-det].

[18] I. Israelashvili et al. "Fast-neutron and gamma-ray imaging with a capillary liquid xenon converter coupled to a gaseous photomultiplier". In: *JINST* 12.09 (2017), P09029. DOI: 10.1088/1748-0221/12/09/P09029. arXiv: 1707.04794 [physics.ins-det].

[19] M. Cortesi et al. "Concept of a novel fast neutron imaging detector based on THGEM for fan-beam tomography applications". In: *Journal of Instrumentation* 7.2 (2012), p. C02056. DOI: 10.1088/1748-0221/7/02/C02056. arXiv: 1203.0181 [physics.ins-det].

[20] J. Agarwala et al. "The novel photon detectors based on MPGD technologies for the upgrade of COMPASS RICH-1". In: *PoS* MPGD2017 (2019), p. 052. DOI: 10.22323/1.322.0052. arXiv: 1804.05765 [physics.ins-det].

[21] C. Chatterjee et al. "Nanodiamond photocathodes for MPGD-based single photon detectors at future EIC". In: *6th International Conference on Micro Pattern Gaseous Detectors (MPGD2019) La Rochelle, France, May 5-10, 2019*. 2019. arXiv: 1908.05058 [physics.ins-det].

[22] S Bressler et al. "Beam studies of novel THGEM-based potential sampling elements for Digital Hadron Calorimetry". In: *Journal of Instrumentation* 8.07 (2013), P07017–P07017. DOI: 10.1088/1748-0221/8/07/p07017.

[23] K. Mavrokoridis et al. "First Demonstration of Imaging Cosmic Muons in a Two-Phase Liquid Argon TPC using an EMCCD Camera and a THGEM". In: *JINST* 10.10 (2015), P10004. DOI: 10.1088/1748-0221/10/10/P10004. arXiv: 1507.06586 [physics.ins-det].

[24] L. Arazi et al. "First results of a large-area cryogenic gaseous photomultiplier coupled to a dual-phase liquid xenon TPC". In: *JINST* 10.10 (2015), P10020. DOI: 10.1088/1748-0221/10/10/P10020. arXiv: 1508.00410 [physics.ins-det].

[25] D. Hollywood et al. "ARIADNE - A Novel Optical LArTPC: Technical Design Report and Initial Characterisation using the CERN T9 Testbeam and Cosmic Muons". In: (2019). arXiv: 1910.03406 [physics.ins-det].

[26] M. Gai et al. "Toward application of a Thick Gas Electron Multiplier (THGEM) readout for a dark matter detector". In: *23rd Winter Workshop on Nuclear Dynamics (WWND 2007) Big Sky, Montana, February 11-18, 2007*. 2007. arXiv: 0706.1106 [physics.ins-det].

[27] Jia-Qing Yan et al. "Simulation and performance study of ceramic THGEM". In: *Chin. Phys.* C39.6 (2015), p. 066001. DOI: 10.1088/1674-1137/39/6/066001. arXiv: 1408.1780 [physics.ins-det].

[28] Rui de Olivera and Marco Cortesi. "First performance evaluation of a Multi-layer Thick Gaseous Electron Multiplier with in-built electrode meshes—MM-THGEM". In: *JINST* 13.06 (2018), P06019. DOI: 10.1088/1748-0221/13/06/P06019. arXiv: 1804.04643 [physics.ins-det].

[29] F. V. Böhmer et al. "Simulation of Space-Charge Effects in an Ungated GEM-based TPC". In: *Nucl. Instrum. Meth.* A719 (2013), pp. 101–108. DOI: 10.1016/j.nima.2013.04.020. arXiv: 1209.0482 [physics.ins-det].

[30] B. Surrow et al. "Development of tracking detectors with industrially produced GEM foils". In: *Nuclear Instruments and Methods in Physics Research Section A: Accelerators, Spectrometers, Detectors and Associated Equipment* 572.1 (2007). Frontier Detectors for Frontier Physics, pp. 201 –202. ISSN: 0168-9002. DOI: https://doi.org/10.1016/j.nima.2006.10.357. URL: http://www.sciencedirect.com/science/article/pii/S0168900206020572.

[31] B. Azmoun et al. "A Study of Gain Stability and Charging Effects in GEM Foils". In: *2006 IEEE Nuclear Science Symposium Conference Record* 6 (2006), pp. 3847–3851.

[32] M. Alfonsi et al. "Simulation of the dielectric charging-up effect in a GEM detector". In: *Nuclear Instruments and Methods in Physics Research Section A: Accelerators, Spectrometers, Detectors and Associated Equipment* 671 (2012), pp. 6 –9. ISSN: 0168-9002. DOI: https://doi.org/10.1016/j.nima.2011.12.059.

[33] M. Cortesi et al. "THGEM operation in Ne and Ne/CH_4". In: *Journal of Instrumentation* 08.8 (2009), p. 08001. DOI: 10.1088/1748-0221/4/08/P08001. arXiv: 0905.2916 [physics.ins-det].

[34] Marco Cortesi et al. "Studies of THGEM-based detector at low-pressure Hydrogen/Deuterium, for AT-TPC applications". In: *Journal of Instrumentation* 10 (Sept. 2015), P09020–P09020. DOI: 10.1088/1748-0221/2015/09/P09020.

[35] Philip Hauer et al. *Study of Charge-Up Processes in Gas Electron Multipliers*. RD51 Meeting, 05.12.2018. URL: https://indico.cern.ch/event/761831/contributions/3234488/attachments/1765655/2866569/RD51_Hauer.pdf.

[36] Dan Shaked Renous et al. "Gain stabilization in Micro Pattern Gaseous Detectors: methodology and results". In: *JINST* 12.09 (2017), P09036. DOI: 10.1088/1748-0221/12/09/P09036. arXiv: 1707.04356 [physics.ins-det].

[37] M. Pitt et al. "Measurements of charging-up processes in THGEM-based particle detectors". In: *JINST* 13.03 (2018), P03009. DOI: 10.1088/1748-0221/13/03/P03009. arXiv: 1801.00533 [physics.ins-det].

[38] P. M. M. Correia et al. "Simulation of gain stability of THGEM gas-avalanche particle detectors". In: *JINST* 13.01 (2018), P01015. DOI: 10.1088/1748-0221/13/01/P01015. arXiv: 1711.02073 [physics.ins-det].

[39] S. Bachmann et al. "Discharge studies and prevention in the gas electron multiplier (GEM)". In: *Nuclear Instruments and Methods in Physics Research Section A: Accelerators, Spectrometers, Detectors and Associated Equipment* 479.2 (2002), pp. 294 –308. ISSN: 0168-9002. DOI: https://doi.org/10.1016/S0168-9002(01)00931-7. URL: http://www.sciencedirect.com/science/article/pii/S0168900201009317.

[40] A. Deisting et al. "Secondary discharge studies in single- and multi-GEM structures". In: *Nuclear Instruments and Methods in Physics Research Section A: Accelerators, Spectrometers, Detectors and Associated Equipment* 937 (Sept. 2019), pp. 168–180. ISSN: 0168-9002. DOI: 10.1016/j.nima.2019.05.057.

[41] P. Gasik. *Discharge Studies with Single- and Multi-GEM Structures in a Scope of the ALICE TPC Upgrade*. URL: https://indico.cern.ch/event/496113/contributions/2008281/attachments/1242032/1827187/gasik_11032016_sparks_RD51.pdf.

[42] C. Garabatos A. Deisting. "Discharge and stability studies for the new readout chambers of the upgraded ALICE TPC". In: *Journal of Instrumentation* 12 (2017). URL: http://stacks.iop.org/1748-0221/12/i=05/a=C05017.

[43] A. Utrobicic et al. "Studies of the delayed discharge propagation in the Gas Electron Multiplier (GEM)". In: *Nucl. Instrum. Meth.* A940 (2019), pp. 262–273. DOI: 10.1016/j.nima.2019.06.018. arXiv: 1902.10563 [physics.ins-det].

[44] V. Peskov and P. Fonte. "Research on discharges in micropattern and small gap gaseous detectors". In: *arXiv e-prints*, arXiv:0911.0463 (2009), arXiv:0911.0463. arXiv: 0911.0463 [physics.ins-det].

[45] L. Lautner et al. "High voltage scheme optimization for secondary discharge mitigation in GEM-based detectors". In: *JINST* 14.08 (2019), P08024. DOI: 10.1088/1748-0221/14/08/P08024. arXiv: 1906.06721 [physics.ins-det].

[46] Eltos S.p.A. Printed Circuit Boards. URL: http://www.eltos.com.

[47] Jinky Agarwala et al. "The novel photon detectors based on MPGD technologies for the upgrade of COMPASS RICH-1". In: *Nuovo Cimento della Societa Italiana di Fisica C* 41 (Apr. 2018). DOI: 10.1393/ncc/i2018-18074-y.

[48] A. Utrobicic et al. "A floating multi-channel picoammeter for micropattern gaseous detector current monitoring". In: *Nuclear Instruments and Methods in Physics Research A* 801 (Nov. 2015), pp. 21–26. DOI: 10.1016/j.nima.2015.08.021.

[49] Eckert Ziegler. *Alpha spectrometry sources*. URL: http://www.ezag.com/fileadmin/ezag/user-uploads/isotopes/isotopes/Isotrak/isotrak-pdf/Product_literature/EZN/04_section04_alpha_spectrometry_sources.pdf.

[50] M.G. Bagliesi et al. "The TOTEM T2 telescope based on triple-GEM chambers". In: *Nuclear Instruments and Methods in Physics Research Section A: Accelerators, Spectrometers, Detectors and Associated Equipment* 617.1 (2010). 11th Pisa Meeting on Advanced Detectors, pp. 134 –137. ISSN: 0168-9002. DOI: https://doi.org/10.1016/j.nima.2009.07.006. URL: http://www.sciencedirect.com/science/article/pii/S0168900209013850.

[51] C. Altunbas et al. "Construction, test and commissioning of the triple-gem tracking detector for compass". In: *Nuclear Instruments and Methods in Physics Research Section A: Accelerators, Spectrometers, Detectors and Associated Equipment* 490.1 (2002), pp. 177 –203. ISSN: 0168-9002. DOI: https://doi.org/10.1016/S0168-9002(02)00910-5. URL: http://www.sciencedirect.com/science/article/pii/S0168900202009105.

[52] P. Gianotti et al. "The Straw Tube Trackers of the PANDA Experiment". In: *Proceedings, 3rd International Conference on Advancements in Nuclear Instrumentation Measurement Methods and their Applications (ANIMMA 2013): Marseille, France, June 23-27, 2013*. 2013. DOI: 10.1109/ANIMMA.2013.6728039. arXiv: 1307.4537 [physics.ins-det].

[53] G. Dellacasa et al. "ALICE: Technical design report of the time projection chamber". In: (2000).

[54] *Upgrade of the ALICE Time Projection Chamber*. Tech. rep. CERN-LHCC-2013-020. ALICE-TDR-016. 2013. URL: http://cds.cern.ch/record/1622286.

[55] R. Veenhof. *Garfield - simulation of gaseous detectors*. 1984 - 2010. URL: http://garfield.web.cern.ch.

[56] Berkin Ulukutlu. *Development of an optical read-out for GEM detector stability studies*. unpublished bachelor thesis. Sept. 2018.

[57] P. Gasik et al. "Charge density as a driving factor of discharge formation in GEM-based detectors". In: *Nuclear Instruments and Methods in Physics Research Section A: Accelerators, Spectrometers, Detectors and Associated Equipment* 870 (2017), pp. 116 –122. ISSN: 0168-9002. DOI: https://doi.org/10.1016/j.nima.2017.07.042. URL: http://www.sciencedirect.com/science/article/pii/S0168900217307878.

[58] S. Agostinelli et al. "Geant4—a simulation toolkit". In: *Nuclear Instruments and Methods in Physics Research Section A: Accelerators, Spectrometers, Detectors and Associated Equipment* 506.3 (2003), pp. 250 –303. ISSN: 0168-9002. DOI: https://doi.org/10.1016/S0168-9002(03)01368-8. URL: http://www.sciencedirect.com/science/article/pii/S0168900203013688.

[59] *G4EmLivermorePhysics*. 2018. URL: https://geant4.web.cern.ch/node/1619.

[60] *Addendum to the Technical Design Report for the Upgrade of the ALICE Time Projection Chamber*. Tech. rep. CERN-LHCC-2015-002. ALICE-TDR-016-ADD-1. 2015. URL: http://cds.cern.ch/record/1984329.

[61] L. Rolandi W. Blum. *Particle Detection with Drift Chambers*. Springer-Verlag, Berlin, New York, London, 1993.

[62] A. Breskin et al. "A concise review on THGEM detectors". In: *Nuclear Instruments and Methods in Physics Research Section A: Accelerators, Spectrometers, Detectors and Associated Equipment* 598.1 (2009), 107–111. ISSN: 0168-9002. DOI: 10.1016/j.nima.2008.08.062. URL: http://dx.doi.org/10.1016/j.nima.2008.08.062.

[63] A. Mathis and L. Lautner. *DischargeSim*. URL: https://github.com/llautner/discharge_sim.

[64] Rene Brun and Fons Rademakers. "ROOT — An object oriented data analysis framework". In: *Nuclear Instruments and Methods in Physics Research Section A: Accelerators, Spectrometers, Detectors and Associated Equipment* 389.1 (1997). New Computing Techniques in Physics Research V, pp. 81 –86. ISSN: 0168-9002. DOI: https://doi.org/10.1016/S0168-9002(97)00048-X. URL: http://www.sciencedirect.com/science/article/pii/S016890029700048X.

[65] Fabio Sauli. "The gas electron multiplier (GEM): Operating principles and applications". In: *Nuclear Instruments and Methods in Physics Research Section A: Accelerators, Spectrometers, Detectors and Associated Equipment* 805 (2016). Special Issue in memory of Glenn F. Knoll, pp. 2 –24. ISSN: 0168-9002. DOI: https://doi.org/10.1016/j.nima.2015.07.060. URL: http://www.sciencedirect.com/science/article/pii/S0168900215008980.

[66] COMSOL AB Stockholm Sweden. *COMSOL Multiphysics®v. 5.2.* URL: www.comsol.com.